

A Squall Line in Southern Germany: Kinematics and Precipitation Formation as Deduced by Advanced Polarimetric and Doppler Radar Measurements

P. F. MEISCHNER, V. N. BRINGI,* D. HEIMANN AND H. HÖLLER

DLR, Institut für Physik der Atmosphäre, Oberpfaffenhofen, Federal Republic of Germany

(Manuscript received 16 March 1990, in final form 24 July 1990)

ABSTRACT

A multiscale analysis of a squall line system is reported in this paper. It is shown that the squall line was initiated as part of a synoptic-scale frontal zone. The main emphasis then is on the polarimetric and Doppler radar measurements which give insight into the meso- and microscale structure of the kinematics and the precipitation microphysics especially within the new cells growing ahead of the squall line, and within the main precipitation system. The principal polarimetric measurements considered are the differential reflectivity (Z_{DR}) and a related new derived parameter termed the difference reflectivity or Z_{DP} which is useful in detection of rain-ice mixed phase precipitation. A limited amount of time series data have been analyzed to derive the specific differential phase (K_{DP}) and the backscatter differential phase (δ) between horizontal and vertical polarizations. A brief overview of the microphysical interpretation of these parameters is provided. The newly grown clouds are identified as positive Z_{DR} columns, i.e., regions of low reflectivity and unusually large Z_{DR} . Within the high reflectivity part of the squall line, intense precipitation in the form of raindrops mixed with small, melting hail may be inferred. The radar observations were shown to be in good agreement with a hail melting model. A conceptual model of the squall line is provided based on the Doppler and polarimetric data. It demonstrates the internal circulation structure as well as the contribution of melting ice particles to the cold pool dynamics.

1. Introduction

Squall lines are highly organized, long lasting, mesoscale thunderstorm complexes. Tropical and mid-latitude lines have been observed and analyzed in a number of case studies. The general structure is found to be similar for all cases, e.g., the steady-state principal airflow pattern and the time scales observed. The main characteristic is a line of deep convective cells some 100 km in length forming the leading edge of the system. In a mature state this line of cumulonimbus clouds being connected with severe weather events is followed by an adjacent region of widespread stratiform precipitation. This stratiform region lasts longer than the line of deep convective activity by several hours. The life cycle of the whole system extends from about 6 to more than 15 hours.

The main airflow pattern is generally two-dimensional in structure at least for scales larger than the individual convective cells. The main inflow occurs from the front side, where ground-level moist and un-

stable air is forced to be directed into a more upward motion causing the line of deep convective activity. Downward motion is connected with: 1) the mesoscale cool and rather stable air moving in a broad sometimes jetlike flow from rear-to-front, and 2) the line of deep convection that enhances the precipitation laden downdrafts and locally intensifies the forward density current at the ground. This latter mechanism plays an important role in maintaining the long lasting, steady-state structure of squall lines.

Although this general structure has been observed and described for a number of case studies, important differences are reported. The kinematical and thermodynamical structures of several tropical squall lines have been analyzed by Roux et al. (1984), Chong et al. (1986), and Roux (1987). Model simulations by Redelsperger and Lafore (1987) for one typical case of these observations resulted in circulation patterns, comparable with the observed ones but differing in intensity as a consequence of the forcing mechanisms. Best agreement of circulation pattern, system propagation velocity, and precipitation rate were obtained if a mesoscale, midlevel, rear inflow jet was included in the calculations. The line of deep convection was composed of relatively short-lived cells. Between the convective cells, intrusions of low equivalent potential temperature air or downdraft cells were found. They contribute in feeding the forward gravity current near the ground. The simulations further showed that for

* Department of Electrical Engineering, Colorado State University, Fort Collins, Colorado.

Corresponding author address: Dr. P. F. Meischner, DLR, Institut für Physik der Atmosphäre, D-8031 Oberpfaffenhofen, Federal Republic of Germany.

the line of deep convection the two-dimensional structure at low level becomes progressively three-dimensional with height above 2 km, allowing a crossing and hence a mixing of the two inflow layers of high and low equivalent potential temperature. This "cross-over zone" extends between 2 and 6 km as first described by Zipser (1977) and Betts (1976).

A study comparing 18 squall line cases with trailing stratiform precipitation including composites for a number of similar events has been presented by Smull and Houze (1987). Tropical, as well as, midlatitude systems were included. The relative airflows and accompanying precipitation structures were examined with emphasis on the occurrence of "rear inflows." The intensity of this rear inflow has been hypothesized to play an important role in maintaining the steady-state structure. Three distinct classes were identified: the "strong rear inflow" cases characterized by flows crossing the back edge of the stratiform precipitation area with relative speeds exceeding 10 m s^{-1} , the "weak rear inflow" cases with velocities between 5 and 10 m s^{-1} , and the "stagnation zone" squall line systems with rear inflow velocities of less than 5 m s^{-1} relative to the system. From these studies it is concluded that physical processes internal to the mesoscale system are generating rear-to-front flow behind the convective line without the aid of ambient flow entering the storm. One explanation is a hydrostatically induced perturbation pressure minimum that develops immediately under or behind the rearward sloped, warm convective updrafts. Further, within the stratiform region a mid-level mesolow may develop due to the combined effect of latent heat release aloft by ascent and freezing of supercooled water and evaporative cooling as stratiform precipitation falls through subsaturated air (Brown 1979).

A recent theory for strong, long-lived squall lines (Rotunno et al. 1988) addresses the question whether a squall line is a system of special long-lived cells or whether it is a long-lived system of ordinary, short-lived cells. The majority of cases observed indicate that the latter is a consistent hypothesis. The numerical experiments however show that either type may develop from a linelike initial linelike disturbance. A key parameter of this theory is shown to be a shallow shear, oriented more or less perpendicular to the line. The interaction of the storm cell's cold outflow at the surface with the low-level shear produces much deeper lifting than would be possible without the low-level shear. Lines of more-or-less ordinary cells that continually grow and decay occur under conditions of strong shear at low levels directed perpendicular to the line with weak shear aloft. Lines of really steady supercells occur with strong, deep shear oblique to the line, which allows the three-dimensional circulation within each cell to persist without interference from its neighbors. These general findings have been confirmed by three-dimensional model simulations by Weisman et al. (1988).

They found that the structures of the simulated squall lines are most sensitive to the magnitude of the shear component perpendicular to the line. The optimal conditions for deep lifting and therefore longevity and overall system strength are found to be the balance between the developing cold pool, which induces an upshear-tilted circulation, and the strength of the ambient low-level shear ahead of the line. In the experiments a velocity change of $15\text{--}25 \text{ m s}^{-1}$ over the lowest 2.5 km AGL turned out to be the optimum.

The squall line systems observed in the tropics and at midlatitudes so far have been analyzed and described mainly with respect to their thermodynamical, dynamical, and kinematical structures. It is the goal of this paper 1) to present radar analysis of a squall line observed in southern Germany on 1 July 1987, and 2) to discuss its kinematics and severe weather events such as hail and a downburst connected with the line of deep convection.

The main observations have been performed with the advanced polarimetric Doppler radar located in Oberpfaffenhofen. It is especially the polarimetric capability of this radar that provided insights into the precipitation and hail formation processes. Polarimetric measurements analyzed are differential reflectivity (Z_{DR}) and a new parameter termed difference reflectivity or Z_{DP} . These data are obtained in the so-called fast reflectivity operating mode of the radar. Limited time series data were also gathered from which the specific differential phase (K_{DP}) and the backscatter differential phase (δ) are derived. A brief overview of the microphysical interpretation of these polarimetric observables in rainfall is provided. Detailed interpretation of polarimetric radar data in two distinct areas of the squall line have been provided, i.e., the main precipitation core, and the low-reflectivity clouds along the inflow region. The Rasmussen–Heymsfield (1987a) hail melting model is used as a framework to interpret vertical profiles of polarimetric data within the main precipitation core.

2. The DLR polarimetric diversity Doppler radar, POLDIRAD

The main characteristics of the DLR cloud physics radar comprise the polarization agility for transmitting, the dual-channel receiving, the advanced Doppler capability, and the real time processing and display. A selection of two parameters out of the following are available for real time display: reflectivity factor for each polarization of choice; the differential reflectivity; and the depolarization ratio for a selected polarization, especially the linear depolarization ratio; or the circular depolarization ratio; the Doppler velocities; and the Doppler spectral widths for both receiving channels. Time series data are recorded for off-line analysis. The system has been described in detail elsewhere—see Schroth et al. (1988), Meischner (1989)—therefore,

TABLE 1. POLDIRAD Characteristics.

Wavelength (cm)	5.45
Beamwidth (deg)	1.0
Peak power (kW)	400 (adjusted)
Pulse repetition frequency (Hz)	variable from 160 to 2400
Pulse width (μ s)	0.5, 1, 2
Number of samples	32, 64, or 128
Range bins	452, flexible bin spacing
Range resolution (m)	Any multiple of 75. 75: unambiguous range 60 km. 150: unambiguous range 120 km. 300: unambiguous range 300 km
Antenna gain (dB)	44.5
Sidelobe level (dB)	<32 (for linear polarization)
Cross-polarization level (dB)	<28
Polarizations	variable (linear, circular, elliptic) 128 amplitude and phase settings
Receiver	2 channels linear and logarithmic
Minimal detectable signal (dBm)	-108, for 0.5- μ s pulse width
Processed parameters available for on line display	Reflectivity: < ± 1 dB precision, relative precision ± 0.1 dB Radial velocity: < ± 1 m s ⁻¹ precision, receiver bandwidth 4.8 MHz, unambiguous interval ± 32 m s ⁻¹ Doppler spectral width: < ± 1 m s ⁻¹ precision Differential reflectivity: precision 0.2 dB Linear depolarization ratio: precision ~ 0.2 dB Circular depolarization ratio: precision ~ 0.2 dB

only the main characteristics are summarized in Table 1.

Different modes of operating the system are selectable via the operator terminal. The Doppler mode provides reflectivity, Doppler velocity, and Doppler spectral width, while the fast reflectivity mode provides reflectivity, differential reflectivity, depolarization ratios, and a hail signal (see Meischner 1989). Full Doppler spectrum information, mainly for archiving, is available with the spectrum mode. For archiving scattering matrix elements and the display of all polarimetric parameters, the matrix mode must be selected. Selection of operating modes, scan, and display parameters (two radar observables can be displayed simultaneously) and their adjustments based on the observed weather events are possible via the terminal in about one minute. In this paper data from three operating modes are analyzed, 1) the Doppler mode with transmit polarization fixed at linear vertical (V), 2) the fast reflectivity mode with the transmit polarizations switched between horizontal (H) and vertical (V) states on a pulse-to-pulse basis permitting measurements of Z_{DR} , and 3) a time series mode permitting measurements of Z_{DR} , K_{DP} , and δ .

3. Synoptic-scale environment

On 1 July 1987 a cold front approached southern Germany from the northwest (Fig. 1a). The 0000 UTC analysis shows a preceding convergence line approximately 200 km ahead of this cold front. The upper-level trough followed the front from the British Isles (Fig. 1b). When the trough approached, the upper-level flow over southern Germany turned to the southwest.

The large-scale stratification is illustrated by the vertical profile over Munich (Fig. 2) and a NW-SE cross section from Long Kesh (United Kingdom) to Budapest (Hungary) (Fig. 3), both at 1200 UTC. At this time, the convergence line is situated just east of "Stuttgart," and the surface cold front is near "Idar-Oberstein." The hatched area in Fig. 3 indicates a decrease of the equivalent potential temperature (θ_e) with height and consequently potential instability. This zone extends up to 4 km MSL. This situation is caused by high moisture around the 2-km height and dry air aloft. The static stability is rather weak ($\partial\theta/\partial z = 3$ K km⁻¹ over Munich between 2 and 10 km MSL).

One can hardly estimate whether the 1200 UTC sounding of Munich is representative for the closer environment of the squall line that developed along the large-scale convergence line. The sounding was taken approximately four hours before the squall line passed over Munich, and might have been modified by horizontal advection, lifting, or latent heat conversions. The 1200 UTC sounding of Stuttgart (not shown) was taken shortly after the squall line's passage. Compared to the Munich sounding it shows lower temperatures around 3000 m MSL. The equivalent potential temperature (θ_e), however, does not show a significant difference. Therefore, the squall line is an air-mass internal structure. Above 3000 m MSL, the temperature profiles over both locations do not differ much. Presumably the warming due to the latent heat release was compensated by prefrontal cold air advection, which is indicated by a counterclockwise veering of the winds within the troposphere.

Mesoscale analyses of the surface fields have been performed every three hours. The map of 1200 is pre-

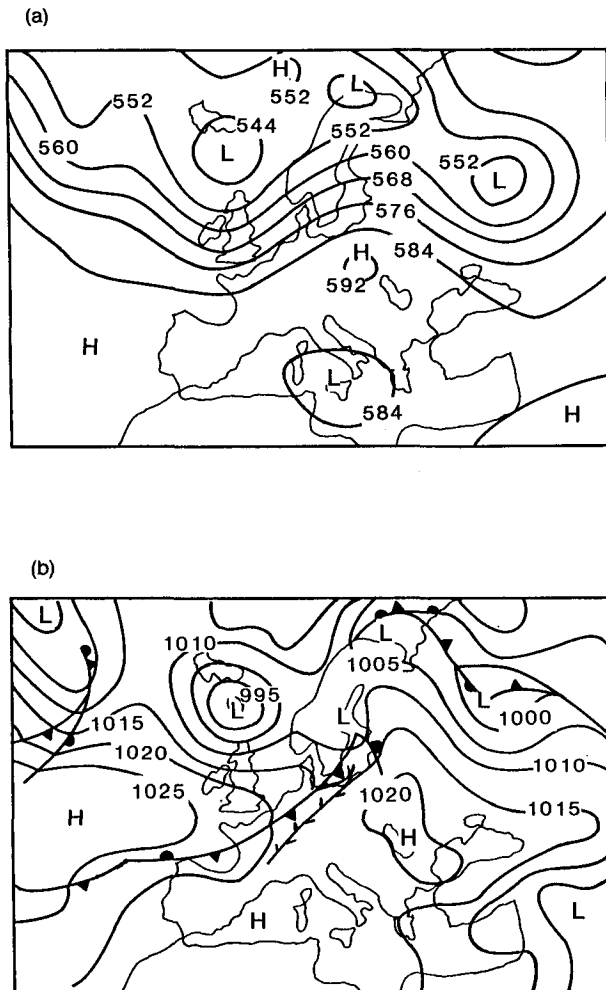


FIG. 1. Synoptic situation of 1 July 1987 at 0000 UTC. (a) Absolute topography (labels in dam) of the 500-hPa level and (b) Surface weather map (pressure reduced to MSL labeled in hPa).

sented as Fig. 4. It shows a rather complex structure ahead and behind the large-scale cold front (CF), consisting of convergence lines (CL1, . . . , CL5) and squall lines (SL1 and SL2). By convergence lines, lines of surface wind convergence are denoted. They coincide with low pressure troughs and favor the development of local showers or thunderstorms. They are almost undetectable in the temperature field. The term squall line signifies thunderstorms organized in a line, which forms the leading edge of a cold air pool. They are associated with a significant drop of temperature and a strong increase of pressure at their rear side. They do not appear in the field of the equivalent potential temperature.

This study exclusively focuses on squall line SL2. It developed about 200 km east of the cold front (CF) at the eastern side of an area of enhanced prefrontal convective activity after the thunderstorm outflows had formed a pool of cold air. The squall line moved south-

eastward accompanied by a temperature drop and a pressure rise. Near the Alps the cold air was hindered to spread out to the south. Trapped by the mountains the air now followed the pressure gradient towards the east. The squall line increased its eastward component of propagation speed from 14 (between 1200 and 1500 UTC) to 20 m s^{-1} (between 1500 and 1800 UTC).

4. The area of deep convection

a. Kinematics

For discussing the airmass flow especially for the leading edge of the squall line this study concentrates on a selected area of approximately 60 km along the N-S direction by 40 km perpendicular to the line when the system moving from west to east arrived at a position 60 km west of Oberpfaffenhofen (OP). The knowledge of the airflow pattern not only gives insight into the underlying dynamics but is of importance for understanding the precipitation formation process, especially the hail growth.

Figure 5a-c show a sequence of sector PPIs west of OP at elevation angles of 1.3°, 4.8°, and 8.8°, respectively, at 1314:49 UTC. The Doppler velocity is depicted on the left and the reflectivity on the right. This selected sequence shows that heavy precipitation reaches the ground within the first 5 to 10 km from the leading edge of the line and that the line of precipitation is structured into different shafts. The strong precipitation shafts in the southern part of this sector extend up to midlevels only. They are tilted slightly westwards. This part represents dissipating cells with falling precipitation parcels. The northern part displays a vigorously active cell with a high and upright core of high reflectivities of more than 50 dBZ up to 10 km AGL (above ground level).

The different states in the life cycles of the northern and southern cells are connected with different Doppler patterns. The Doppler velocities shown in the figures are the original ground-relative velocities that have not been corrected for discussing a system relative flow. For considering these effects the west-east propagation velocity of about 6 m s^{-1} has to be added to the values. Near the ground (Fig. 5a) all air moves to the east with distinct gusts of up to 15 m s^{-1} where heavy precipitation hits the ground. At midlevel (Fig. 5b) a distinct line of confluence intersects the row of reflectivity cells centrally. The radial convergence is much stronger for the growing intense northern cell with values up to $2 \times 10^{-3} \text{ s}^{-1}$ indicating a strong inflow. Between the cells, the inflow from east to west impinges deeper into the system, whereas at the cells themselves the inflowing air is forced to more vertical directions. At upper levels (Fig. 5c) a clear line of divergence characterizing the outflow is seen at cloud top in the southern part.

From a volume scan, i.e., a number of PPI scans with increasing elevation angles, a three-dimensional view of the system is constructed and displayed in Fig.

* equivalent-potential temperature + potential temperature

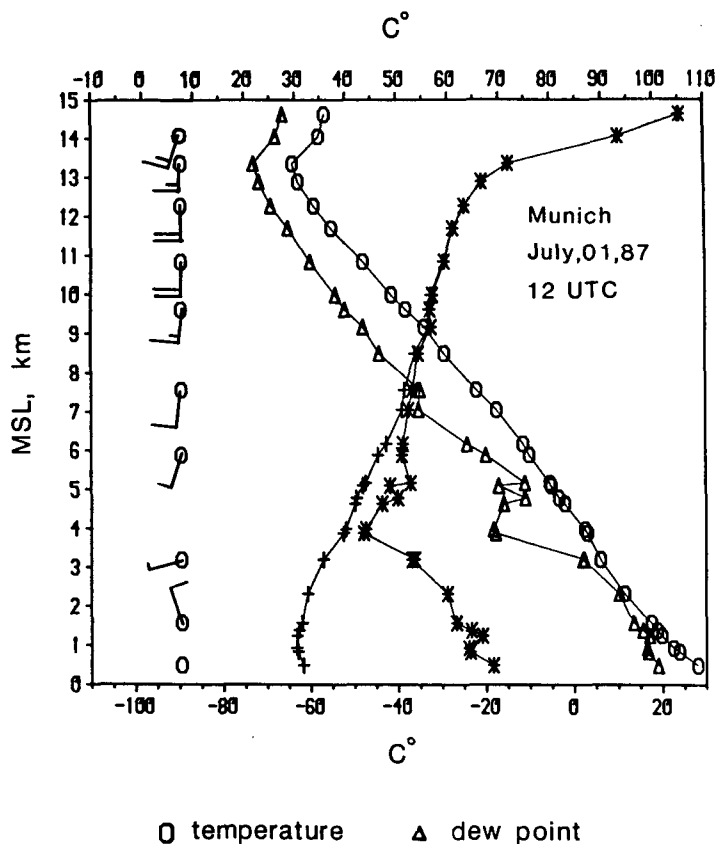


FIG. 2. Vertical profiles as measured by the Munich radiosonde on 1 July 1987 at 1200 UTC. The graph shows temperature (○), dewpoint (△), potential temperature (+), and equivalent potential temperature (*). Wind is given in standard notation (kt).

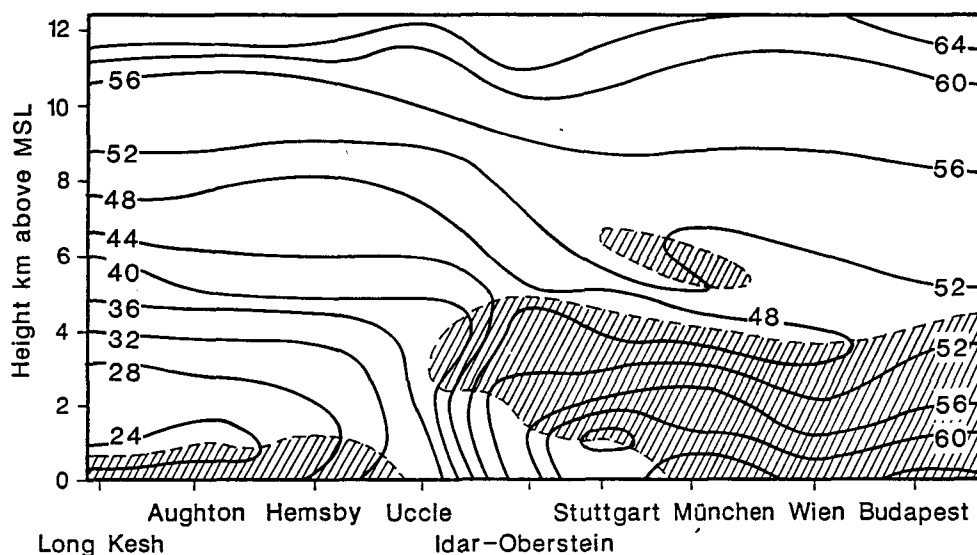


FIG. 3. Vertical cross sections of 1 July 1987 at 1200 UTC. Equivalent potential temperature (labeled in °C). The hatched areas indicate layers of negative $\partial\theta_e/\partial z$, i.e., conditionally unstable layers.

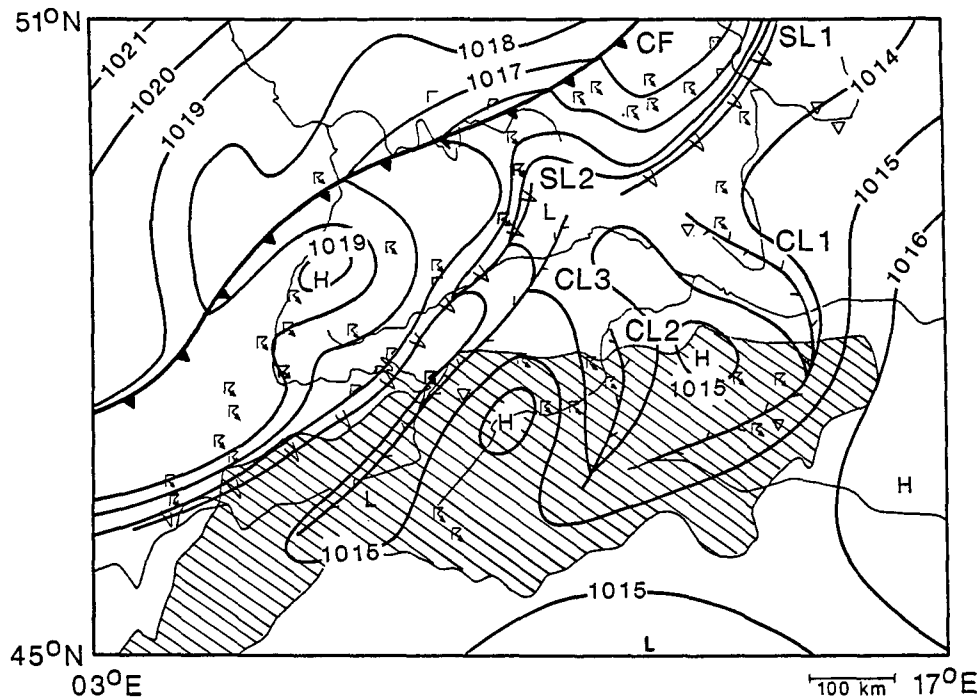


FIG. 4. Mesoscale situation showing pressure reduced to MSL (labeled in hPa), the cold front (CF), convergence lines (CL), and squall lines (SL). Reported showers and thunderstorms are marked using international symbols. The hatched area represents the Alps. Analysis of 1200 UTC 1 July 1987.

6. The coordinates are with respect to OP. For a more clear display the fields of reflectivity, velocity, and turbulence have been thresholded. A row of five precipitating cells, aligned from south to north are distinguishable only because of the separation of the 40-dBZ contour at upper levels. The Doppler measurements clearly show the wedge-shaped volume of air near the ground with a strong Doppler component towards the radar or to the east. The high-level outflow of the southern cells is clearly depicted also. The midlevel inflow from east to west is strengthened by the growing cell in the northern part of this section. The highest turbulence values are connected with the shear regions. The dissipation of turbulent kinetic energy is estimated from measured values of the Doppler spectral width following a suggestion of Istok and Doviak (1986), see also Brewster and Zrnić (1986). For estimating the contribution of shear to the measured Doppler spectral widths, a least squares fit is applied to neighboring velocity measurements, see Meyer and Jank (1989).

The measurements displayed in Fig. 6 show a general two-dimensional flow pattern as discussed in the literature, disturbed by the strong convective cells. A very characteristic cross section, a RHI towards an azimuth of 285° at 1310:40 UTC is depicted in Fig. 7 showing more details. The Doppler velocity field clearly displays the kinematic structure. The wedge-shaped, cool sur-

face air mass moves from west to east with a rather homogeneous Doppler velocity of about 10 m s^{-1} . It is noted from Fig. 5a that a first gust front is visible as a thin echo line at a distance of 30 to 35 km west of OP. Enhanced velocities up to 14 m s^{-1} toward the east are connected with the heavy precipitation shafts at 55 km and with the corresponding gust front at 48 km. The inflow occurs slantwise against and above the cool air from east to west with a rather homogeneous Doppler velocity around 7 m s^{-1} , which corresponds to 13 m s^{-1} relative to the propagating line. It is in this inflow area where by the forced lifting of the moist, unstable boundary layer air entering from the east that deep convection is initiated. The strong reflectivity patterns around 55 km and less distinct near 67 km show a vertical inclination corresponding to the local shear conditions associated with these flow patterns.

The turbulence structure was examined from measurements of the Doppler spectral width (Meischner 1989). The lowest values of ϵ , the rate of the turbulent kinetic energy dissipation, was found within the eastward moving surface air. A value of $\epsilon \approx 0.004 \text{ m}^2 \text{ s}^{-3}$ was estimated. For the shear layer between the eastward and westward moving air mean values of $\epsilon \approx 0.09 \text{ m}^2 \text{ s}^{-3}$ were found. The highest values up to $0.1 \text{ m}^2 \text{ s}^{-3}$ were found within shear regions within the deep and strong convectively active areas.

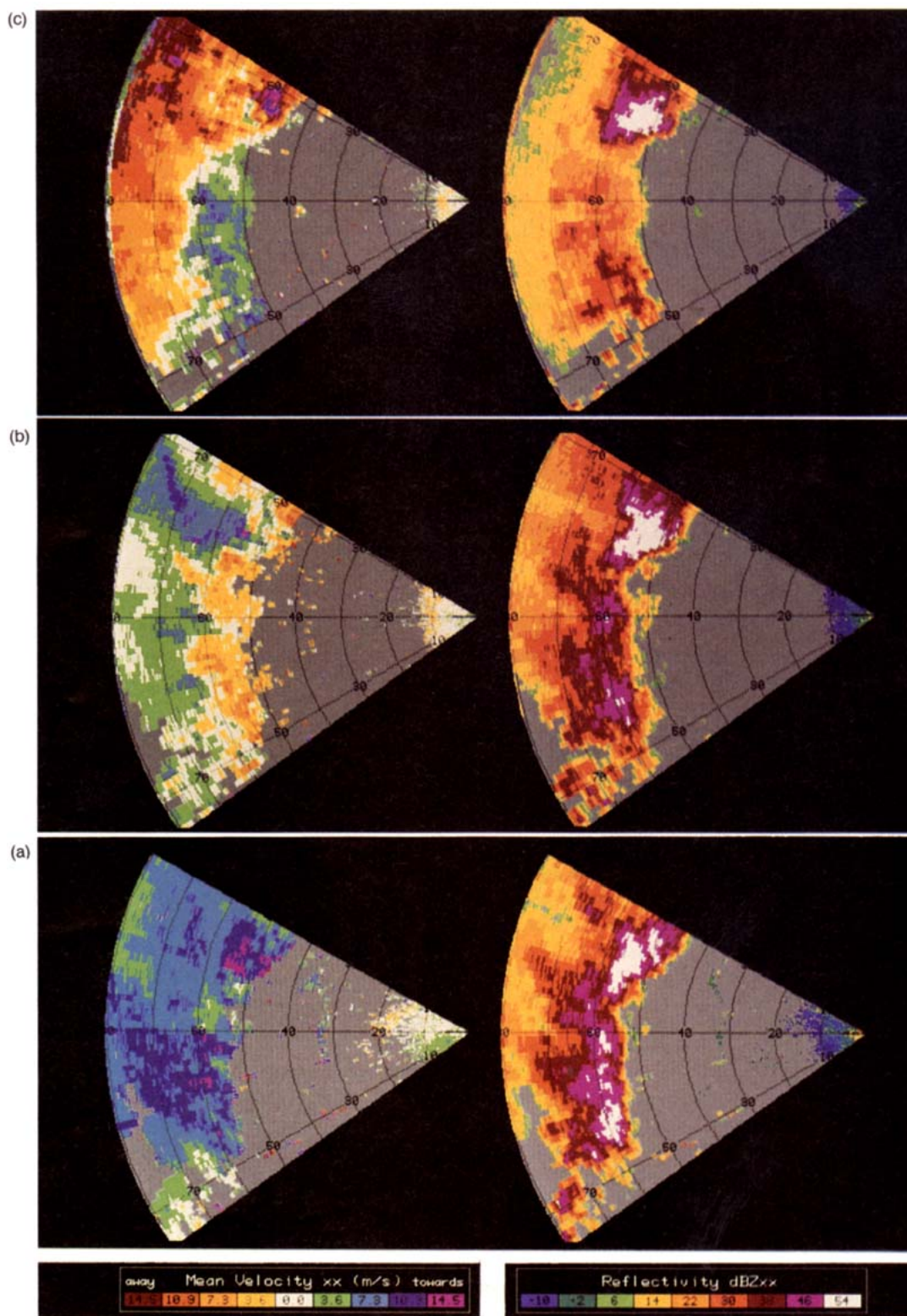
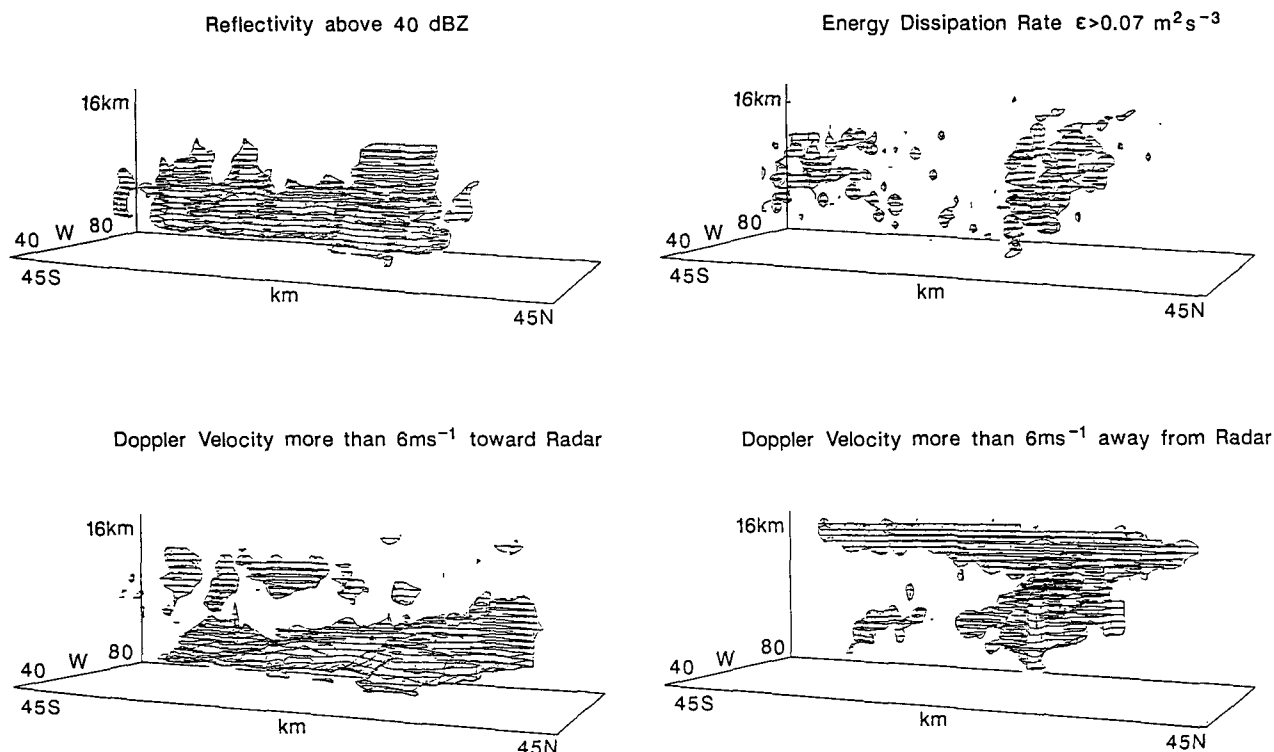


FIG. 5. Sequence of sector PPIs towards the west at elevation angles of (a) 1.3°, (b) 4.8° and (c) 8.8°. Doppler velocity is shown on the left and Z_v (dBZ) on the right side.

SQUALL LINE

July 1, 1987

15 : 06 MEST

FIG. 6. Thresholded fields of reflectivity, Doppler velocity, and ϵ , the rate of dissipation of turbulent kinetic energy.

b. Brief overview of polarimetric observables

It is well known that polarimetric measurements yield significantly new insight into the precipitation process, see for example Hall et al. (1984), Bringi et al. (1984, 1986a,b), Tuttle et al. (1989), Wakimoto and Bringi (1988), and Illingworth et al. (1987). Here measurements of differential reflectivity (Z_{DR}) defined as $10 \log(Z_H/Z_V)$ are reported upon, where $Z_{H,V}$ are the conventional reflectivities at horizontal and vertical polarizations, respectively. A new parameter termed difference reflectivity or Z_{DP} is introduced, which is defined as $10 \log(Z_H - Z_V)$, Golestani et al. (1989). Examples are shown of the specific differential phase (K_{DP} , degrees km^{-1}) and the backscatter differential phase (δ , degrees) obtained from the radar operating in a time series mode. The Mueller (1984) algorithm is used to estimate the propagation differential phase (ϕ_{DP} , degrees) as a function of range from which K_{DP} is derived, Sachidananda and Zrnić (1986).

The microphysical interpretation of Z_{DR} in rainfall is well known, i.e., at long wavelengths it is an excellent estimator of the reflectivity-weighted mean axis ratio of the oblate raindrops filling the radar resolution volume, Jameson (1983). Since, for drops in equilibrium,

the axis ratio is related nearly linearly to the volume equivalent spherical diameter D it is recognized that Z_{DR} is an estimator of mean raindrop size, or of the median volume diameter D_o for an exponential drop-size distribution, Seliga and Bringi (1976), Beard and Chuang (1987). Figure 8a shows calculations at C band of Z_{DR} versus Z_H for a gamma raindrop-size distribution (RSD) of the form,

$$N(D) = N_o D^m \exp[-(3.67 + m)D/D_o]. \quad (1)$$

Ulbrich (1983) has shown that for natural rainfall the parameters (D_o , m , N_o) generally lie in the range,

$$0 < D_o \leq 2.5 \text{ mm},$$

$$-1 < m \leq 4,$$

$$10^{4.2} \exp(2.8m) \leq N_o$$

$$\leq 10^{5.5} \exp(3.57m) \text{ m}^{-3} \text{ mm}^{-1-m}.$$

Each data point in Fig. 8a represents one combination of the triplet of parameters (N_o , D_o , m). The scatter is thus due to fluctuations of the gamma parameters typically found in rainfall. Note that the maximum Z_{DR} for a gamma RSD is around 4 dB, with the parameter variability given above.

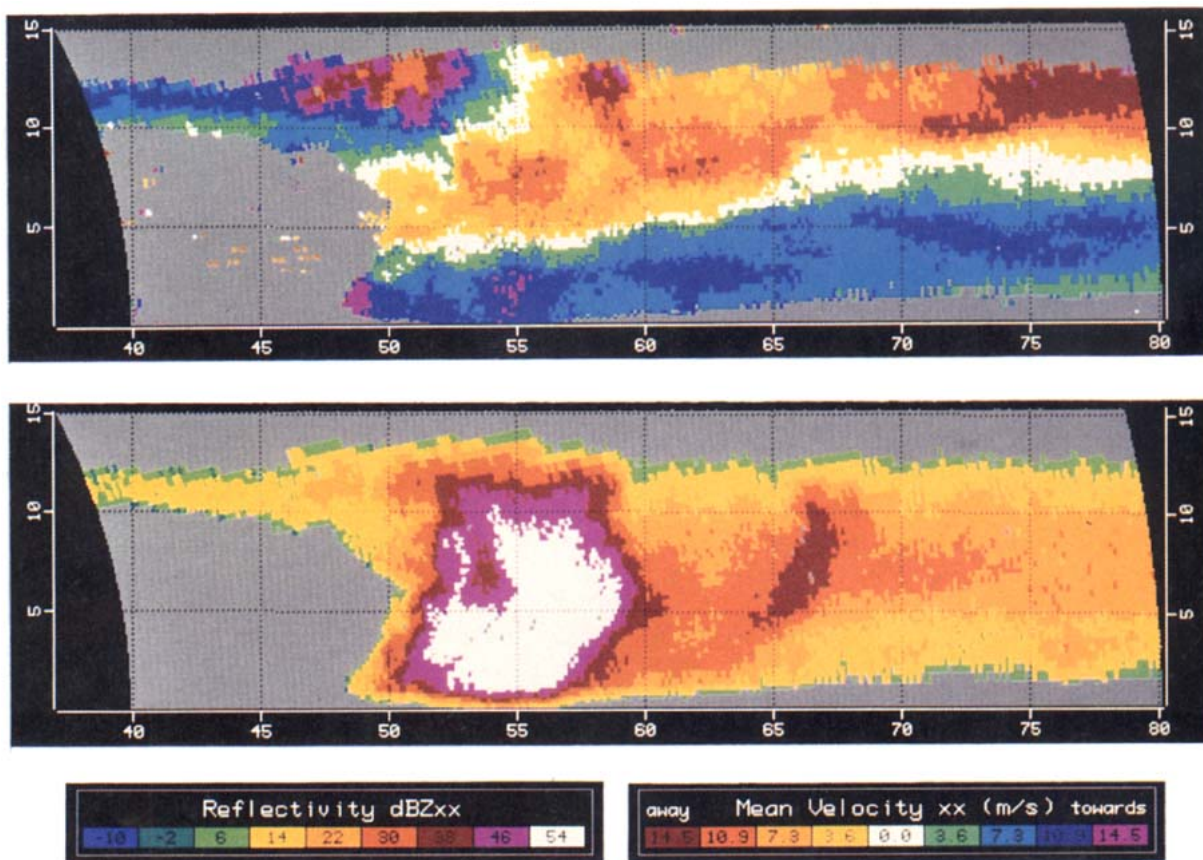


FIG. 7. RHI towards 285° azimuth at 1310:40 UTC showing the Doppler velocity, top and Z_V , bottom.

The usefulness of the new parameter Z_{DP} lies in the fact that it is highly correlated with Z_H in rainfall. Figure 8b shows a scatterplot of Z_{DP} versus Z_H for gamma RSD. Figures 8a,b assume that the equilibrium raindrop shapes are oblate with axis ratio given by Green (1975). This study expects to see that the corresponding radar measurements of Z_{DP} and Z_H will also be highly correlated due to two factors, 1) the high physical correlation for raindrops as seen in Fig. 8b, and 2) the high statistical correlation between the measurement fluctuations in Z_{DP} and Z_H . Thus, deviations from this so-called “rain line” due to mixed-phase precipitation should be clearly visible in the plot of Z_{DP} versus Z_H , see Golestani et al. (1989). Also, a plot of this “deviation from the rain line” with height through different parts of the squall line should reveal the presence of ice or mixed-phase precipitation. Later in this paper plots of this deviation through two different regions of the squall line will be shown, i.e., the inflow region and the main precipitation shaft.

The specific differential phase between H and V polarizations is defined as:

$$K_{DP} = \frac{180}{\pi} \lambda \operatorname{Re} \int [f_H(D) - f_V(D)] N(D) dD \quad (\text{degree km}^{-1}) \quad (2)$$

where λ is the wavelength (5.45 cm) and $f_H(D)$ and $f_V(D)$ are the forward scattering amplitudes for H - and V -polarized waves. The two-way differential propagation phase ϕ_{DP} between ranges r_1 and r_2 is defined as

$$\phi_{DP} = 2 \int_{r_1}^{r_2} K_{DP}(r) dr. \quad (3)$$

At long wavelengths in rainfall it is known that K_{DP} is a good estimator of the D^4 th moment of the RSD, Jameson and Mueller (1985).

The backscatter differential phase shift δ is defined as the argument of the complex number ρ_{HV} where ρ_{HV} is defined as,

$$\rho_{HV} = \frac{\int S_H(D) S_V^*(D) N(D) dD}{\left[\int |S_H(D)|^2 N(D) dD \right]^{1/2} \left[\int |S_V(D)|^2 N(D) dD \right]^{1/2}}. \quad (4)$$

Nonzero values of δ indicate non-Rayleigh scattering effects, McCormick et al. (1979). In (4), S_H , S_V are the principal plane elements of the backscatter matrix

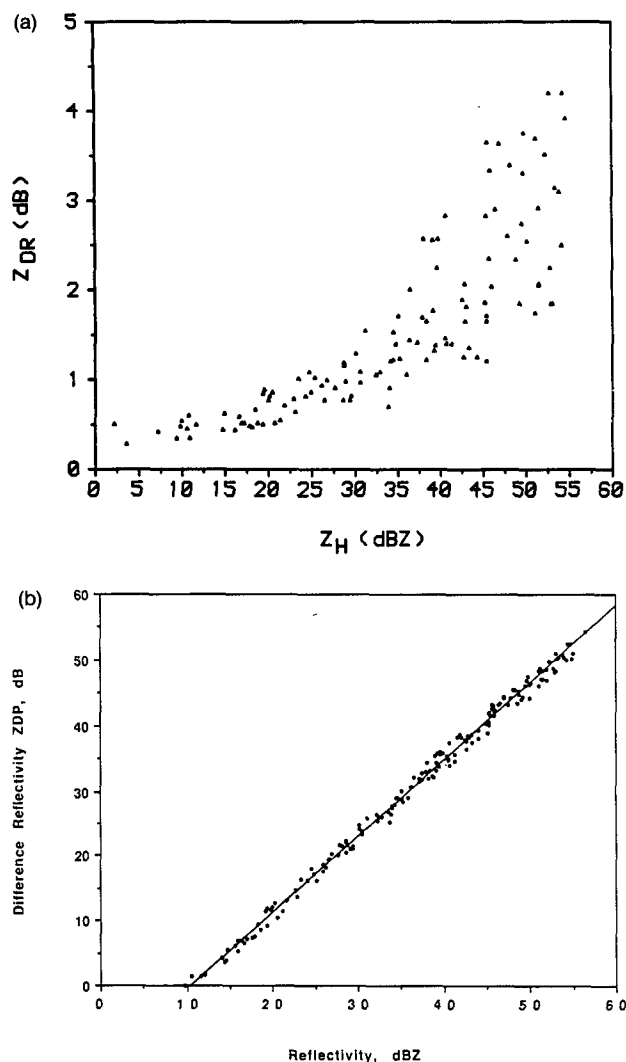


FIG. 8. (a) Computation of C-band differential reflectivity versus reflectivity for gamma raindrop-size distributions. (b) As in (a), except the difference reflectivity Z_{DP} versus Z_H is shown.

at H and V polarizations. Figure 9a shows δ versus Z_{DR} for gamma RSDs. For $Z_{DR} > 3$ dB, the δ values become significant, i.e., spectra with large raindrops at C band fall in the Mie scattering regime. In order to estimate δ from radar measurements, the fact that the Mueller algorithm gives $\phi_{DP} + \delta$ at a given range must be considered. Since ϕ_{DP} is a monotonically increasing function of range in rainfall while δ is not, it is relatively straightforward to estimate δ from the range profile of $\phi_{DP} + \delta$. Figure 9b shows K_{DP} versus Z_H at C band for gamma RSDs. Note the steep increase in K_{DP} near 50 dBZ. Sachidananda and Zrnić (1987) discuss the use of K_{DP} in estimating rain intensity (R).

Illingworth et al. (1987) have reported on positive Z_{DR} columns, i.e., localized areas of positive Z_{DR} extending a few kilometers above the freezing level. Hall

et al. (1984) were the first to suggest that these columns probably contain supercooled raindrops carried up in an updraft, a view that has been confirmed by Tuttle et al. (1989). Caylor and Illingworth (1987) observed unusually high values of Z_{DR} up to 6 dB at S band in early echoes with low reflectivity (10–30 dBZ). These large Z_{DR} values in first echoes have been interpreted as regions of large ($D > 4$ mm) raindrops at very low concentrations ($< 1 \text{ m}^{-3}$).

Similar measurements at C band are reported on here, where unusually large Z_{DR} was measured in low-reflectivity clouds growing in the inflow region just ahead of the squall line. Since the raindrop-size distribution in these clouds tends to be more monodisperse with large raindrop sizes dominating, the Z_H and Z_{DR} values fall outside the range of scatter depicted in Fig. 8a. Figure 10 shows calculations of σ_{DR} , i.e., the Z_{DR} of individual raindrops of equilibrium shape in the size range $4 \leq D \leq 8$ mm at C band. Note the unusually large values of σ_{DR} near $D = 6$ mm. These data may be used to interpret radar measurements obtained from low-reflectivity clouds with unusually large Z_{DR} whose RSDs deviate markedly from the gamma distribution with parameter variations as given by Ulbrich (1983). Thus, Figs. 8 and 9 described previously are applicable for interpreting radar measurements of rainfall within the main precipitation shafts of thunderstorms, while Fig. 10 may be used in cases where unusually high Z_{DR} occurs in clouds with low reflectivity, i.e., the positive Z_{DR} columns.

Dramatic polarimetric signatures are nearly always noted in convective storms near the 0°C level where ice melts to form raindrops, or where hailshafts penetrate to the ground. The shape, orientation, and refractive index distributions of the melting particles govern their polarimetric response. Graupel and hail melting processes have been modeled in detail by Rasmussen and Heymsfield (1987a,b), henceforth referred to as RH. They show that melting processes are significantly affected by initial particle density and size, temperature profile, and relative humidity. Bringi et al. (1986a) used the RH graupel melting model to compute vertical profiles of Z_{DR} which were then compared with radar measured profiles yielding good agreement. They showed that Z_{DR} and its vertical profile below the 0°C level was a good indicator of the onset and progression of melting graupel into raindrops.

The Z_{DR} hail signature in hailshafts has been well documented, especially below the 0°C level by Bringi et al. (1984, 1986b), Illingworth et al. (1986), Aydin et al. (1986), Wakimoto and Bringi (1988), Bringi and Meischner (1988) and Husson and Pointin (1989). Hailstones with $D \geq 10$ mm tend to shed their melt water giving $Z_{DR} \approx 0$ dB or even slightly negative, Bringi et al. (1986b). Thus, in convective storms where spatial separation of hail and rain zones exists then the Z_{DR} hail signature can be easily identified with the hail

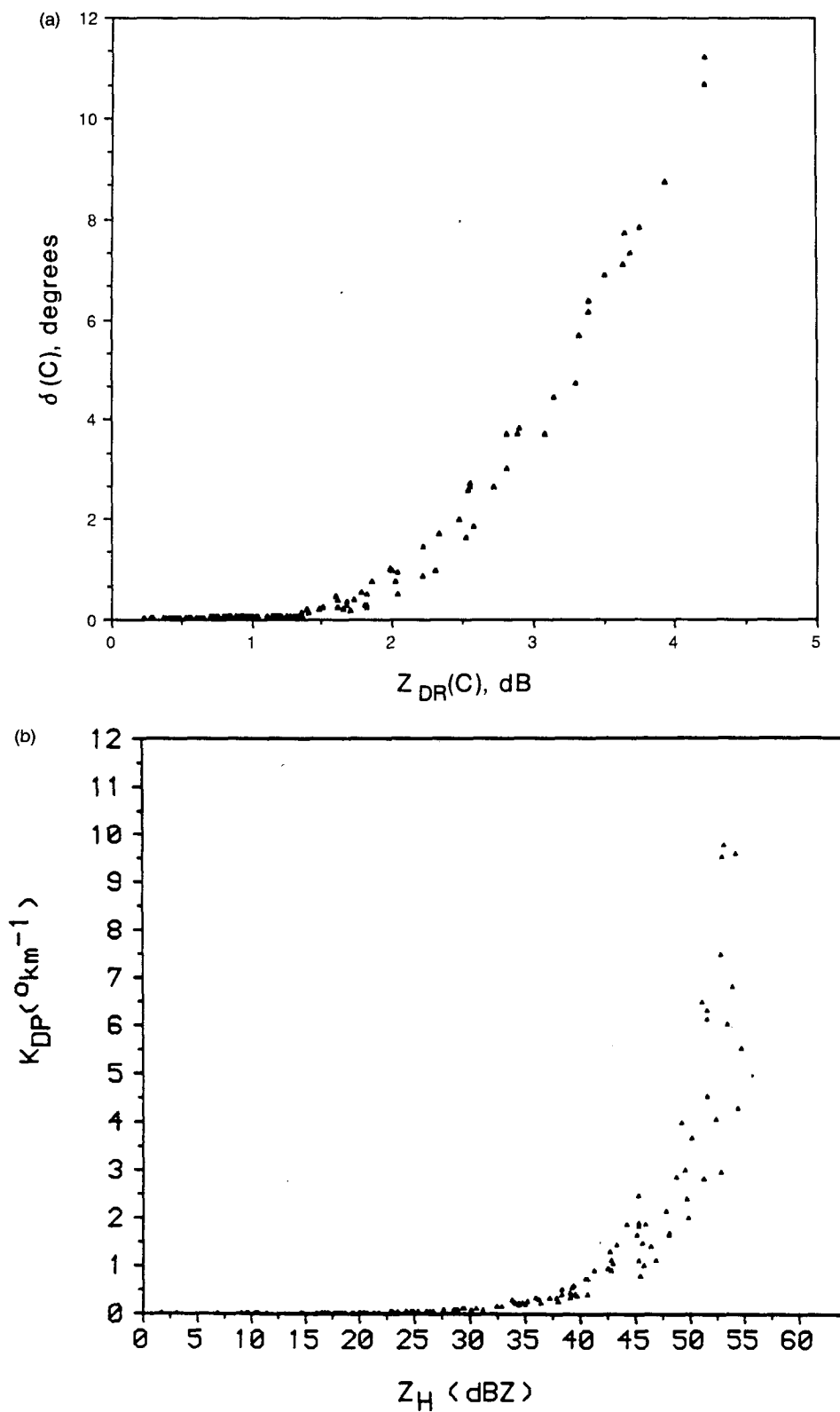


FIG. 9. (a) Computations of C-band backscatter differential phase δ versus Z_{DR} for gamma raindrop-size distributions. (b) As in (a), except differential propagation phase K_{DP} versus reflectivity is shown.

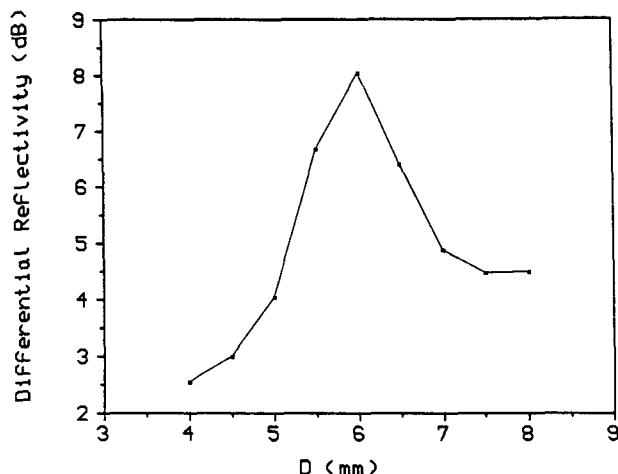


FIG. 10. Differential reflectivity of individual, equilibrium shaped raindrops versus volume-equivalent spherical diameter D .

regions when $Z_{DR} \leq 0$ dB with correspondingly high reflectivity, say, ≥ 50 dBZ. If the hailshaft consists of rain mixed with hail larger than around 10 mm, the Z_{DR} is generally positive but still smaller than would be the case if the total reflectivity were due to raindrops alone. Aydin et al. (1986) have introduced the H_{DR} parameter to account for this where $H_{DR} = Z_H - f(Z_{DR})$ and Z_H is the total reflectivity, while $f(Z_{DR})$ defines a contour on the $(Z_H - Z_{DR})$ plane that forms an upper bound for Z_H values in rain as a function of Z_{DR} . Regions below the 0°C level, where $H_{DR} \geq 0$, define hailshafts. The basic assumption here is that $Z_H \approx Z_V$ for the hail component provided the melt water is shed (hail diameters ≥ 10 mm). This study has introduced a related technique based on the parameter $Z_{DP} = 10 \log(Z_H - Z_V)$ versus Z_H . If the hail is spherical or tumbling then it gives no contribution to Z_{DP} although it does contribute to total Z_H . Thus, rain mixed with hail should have a higher Z_H for a given value of Z_{DP} than rain alone, see Fig. 8b. The same argument also applies to K_{DP} as shown by Zrnica et al. (1989), i.e., the term $f_H(D) - f_V(D)$ in Eq. (2) will be zero for the hail component assuming spherical or tumbling hail. Thus, K_{DP} is only sensitive to the raindrops in mixed-phase precipitation.

Rasmussen and Heymsfield (1987a,b) show that there is a maximum amount of water that can be retained on the surface of a given ice core mass before shedding takes place. If the amount of melt water exceeds the so-called "equilibrium" amount then shedding will occur. Typically, if the initial hail diameter at the 0°C level is less than around 10 mm, then shedding does not occur, rather the melt water forms a torus around the particle equator and upon further melting the particle appears oblate with an inner, spherical ice core surrounded by an oblate shell of melt water. As the ice diameter shrinks to zero, the axis ratio decreases

to that of an equilibrium shaped raindrop of the same volume equivalent diameter. Figure 11 shows a diagram of this melting process derived from the RH model for an initial hail size of 7.3 mm at various heights. As long as the inner ice core exists, the melting hail particle can "look" like a giant raindrop without breaking up, even though its axis ratio may be larger (more spherical) than the equivalent fully melted raindrop. Upon complete melting the largest raindrops ($D = 8$ – 10 mm) may break up spontaneously or as a result of collisions with smaller drops, Beard (1984). If low-density graupel are melting, RH allow the melt water to completely soak the graupel and then melt water accumulates on the surface. If the melt water exceeds the equilibrium amount corresponding to the given ice core mass (which is here the sum of the ice plus any soaked water) then shedding occurs. Thus, the vertical profile of Z_H , Z_{DR} , K_{DP} , and δ should yield insights into the hydrometeor melting process. In addition, the conventional Z_{DR} signature as well as the new parameter Z_{DP} and the associated deviation from the rain line as a function of height should identify mixed phase precipitation.

c. Microphysical interpretation of radar measurements

The squall line system was characterized by three distinct areas. One area was the line of deep convective cells producing heavy rain and hail, the second area was the stratiform region with widespread light rainfall in the rear, and the third area was just ahead of the line of deep convective cells where small clouds were growing in the inflow region. These small clouds appeared as individual cells at low levels but appeared to be joined with the main squall line at upper levels. With time, these feeder clouds merged with the deep convective cells of the squall line. This study concentrates here on the first and third areas.

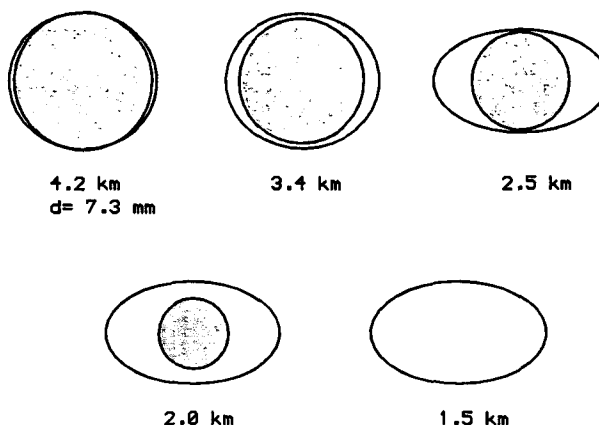


FIG. 11. Diagram of melting hail shapes for initial diameter of 7.3 mm. The various heights MSL are 4.2, 3.4, 2.5, 2.0, and 1.5 km. Inner ice core is spherical and concentric with the oblate particle.

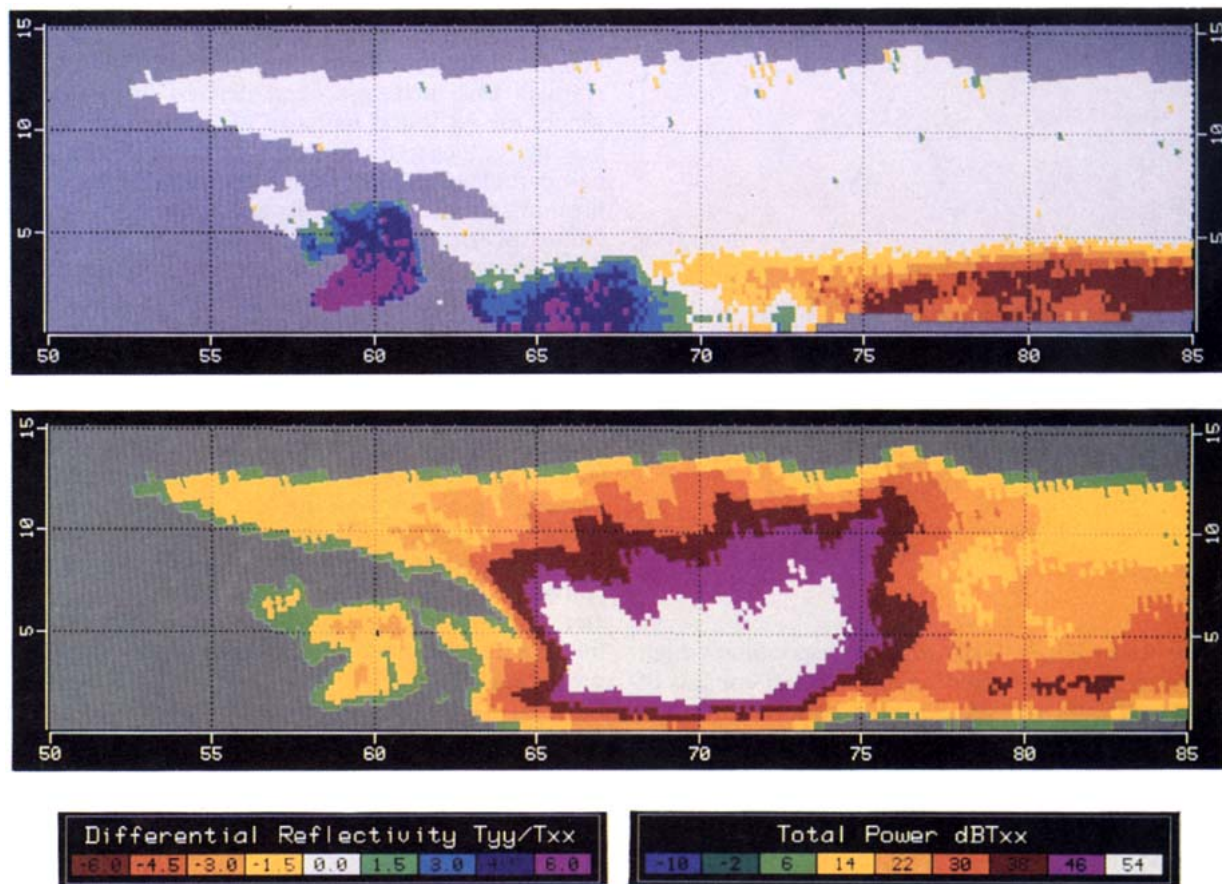


FIG. 12. Vertical cross section (RHI) of T_{VV} the reflectivity or total backscattered power (bottom panel) and Z_{DR} (top panel) taken at 1250:52 UTC along the 274° azimuth (towards the west).

Figure 12 shows a RHI of Z_V and Z_{DR} at 1250:52 UTC taken along the azimuth of 274° . The cumulative decrease in Z_{DR} with increasing range is clearly evident beyond range 68.5 km, the values becoming strongly negative to the far side of the squall line. This steady decrease in Z_{DR} is caused by differential attenuation between the H- and V-polarized waves. The feeder cloud is clearly visible at a range of 60 km with Z_{DR} values up to 6.5 dB and no precipitation reaching the ground. Figure 13 shows a scatterplot of Z_{DR} versus Z_H with data taken from the range interval 58–60 km and from the height interval 2–4 km AGL corresponding to a temperature interval of 12° – 3.5°C . These data constitute unusually high Z_{DR} at very low reflectivities that fall completely outside the expected range for gamma RSDs shown in Fig. 8a. Even at 5 km AGL or -2.5°C , Z_H is in the range 5–15 dBZ and Z_{DR} in the range 1.6–4.5 dB. Thus, this cloud constitutes a positive Z_{DR} column with supercooled raindrops existing up to the 5-km altitude. The feeder cloud appears to be centered on an updraft with vertical air motion large enough to suspend raindrops with monodisperse Z_{DR} (or σ_{DR}) of 5–6 dB, or with diameters in the range 5–

6 mm. The updraft speeds were thus likely to be in the range 10 – 12 m s^{-1} .

For this feeder cloud, which extends about 2 km in horizontal range (from 58–60 km), a Z_{DP} analysis was performed to yield the plot of deviation from the rain line versus height. For example, at a height of 2.34 km AGL or 10.5°C , Fig. 14a shows a scatterplot of $Z_{DP} = 10 \log(Z_H - Z_V)$ versus Z_H . Note the extremely high correlation coefficient of 0.999. Similar plots were constructed at selected heights up to 5.3 km AGL or -5°C . At heights above the 0°C level the correlation coefficient decreases to around 0.95. The deviation from the rain line (which is defined by the line in Fig. 14a) due to ice in the resolution volume is the difference between reference reflectivity of 15 dBZ and the rain component Z_r of Z_H . The quantity Z_r is calculated for each height as follows. First, a scatterplot of Z_{DP} versus Z_H is constructed at a given height and a least squares linear fit is performed. The Z_{DP} value corresponding to the reference reflectivity of 15 dBZ is calculated from this linear fit. This particular Z_{DP} value is used in conjunction with Fig. 14a to determine the corresponding value of Z_r . Finally, the deviation from the rain line

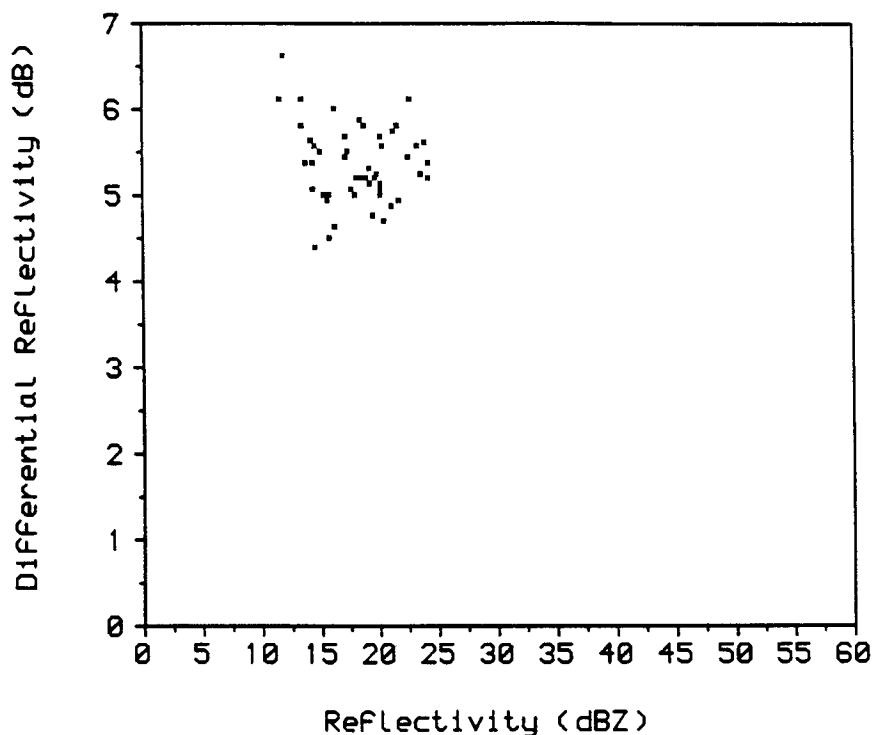


FIG. 13. Scatterplot of Z_{DR} versus Z_H obtained from the radar measurements displayed in Fig. 12. Data shown is from the range interval 58–60 km and in the height interval 2–4 km AGL.

(defined in Fig. 14a) is computed as $15 - Z_r$. A deviation of 3 dB implies that the ratio of the ice reflectivity (in linear units of $\text{mm}^6 \text{m}^{-3}$) to the total reference reflectivity of $10^{1.5} \text{mm}^6 \text{m}^{-3}$ is 0.5. Figure 14b shows

the height profile of this deviation from the rain line for the feeder cloud. A similar procedure was used to calculate the deviation in the main precipitation shaft extending from 66–68 km (see Fig. 12) in range and

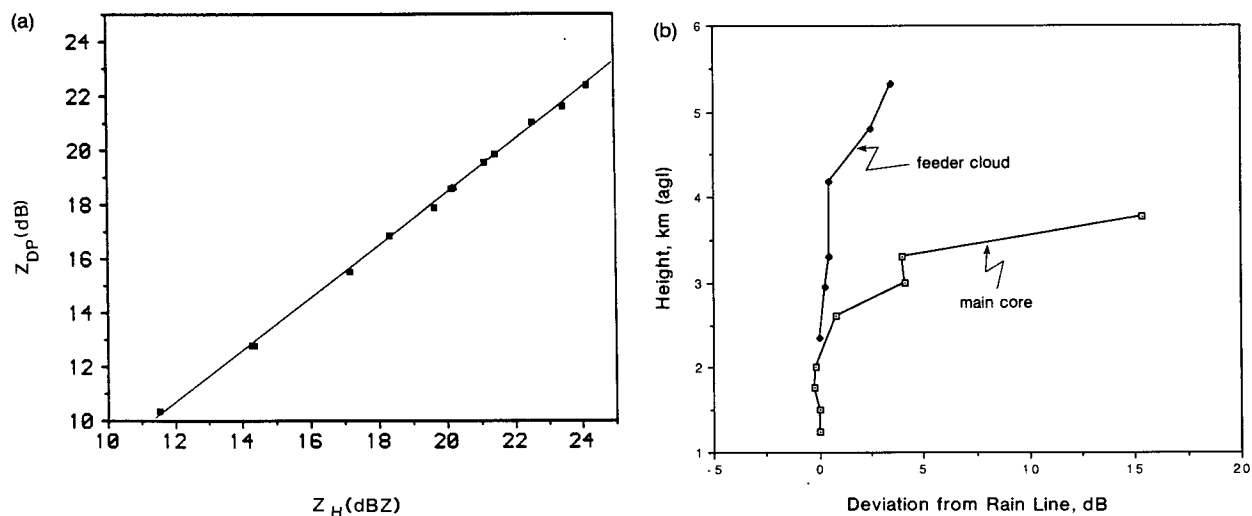


FIG. 14. (a) The difference reflectivity Z_{DP} versus Z_H from radar measurements displayed in Fig. 12. Data taken from the range interval 58–60 km and at a constant height of 2.34 km AGL or 10°C . The solid line is a straight line least squares fit to the data. Correlation coefficient is 0.999. (b) Vertical profile of the deviation from the rain line obtained from the radar measurements shown in Fig. 12. Data for the feeder cloud is taken from the range interval 58–60 km. Data for the main core is taken from the range interval 66–68 km.

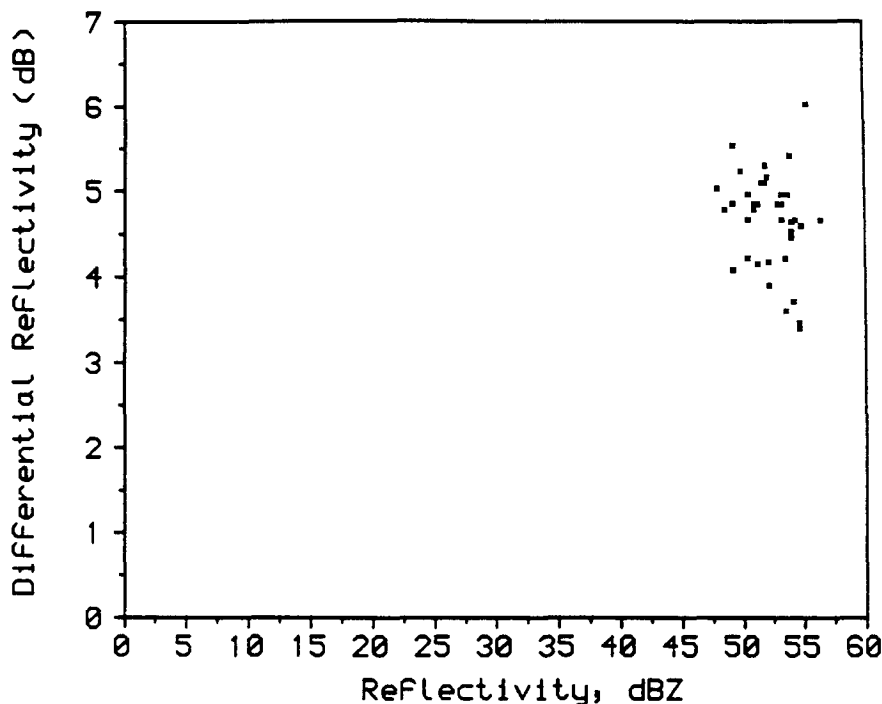


FIG. 15. Scatterplot of Z_{DR} versus Z_H obtained from radar measurements displayed in Fig. 12. Data taken from the range interval 66–68 km and in the height interval 1.5–2.0 km AGL.

in the height interval 1.24–5 km AGL. The deviation from the rain line as a function of height is also shown in Fig. 14b where the reference reflectivity was chosen as 50 dBZ. Note the vast differences between the two profiles marked “feeder cloud” and “main core.” For the feeder cloud the deviation (from rain line) is ~ 0 dB in the height interval 2–4 km AGL above which the deviation increases, more or less linearly, to 3.5 dB at 5.3 km AGL. Thus, it can be inferred that between 2–4 km AGL or 12° – 3.5°C , the particles are all raindrops with a nearly monodisperse distribution of large raindrops of very low concentration, e.g., 1 per 100 m^{-3} of 5-mm diameter raindrops. Above 4.5 km AGL which is close to the 0°C level the deviation from the rain line increases implying the presence of ice (whose origin could not be determined by radar). However, raindrops are still the dominant precipitation type up to the height of 5.3 km or -5°C . Since the feeder cloud occurs on the inflow side of the squall line, the combination of warm cloud base (16°C), sufficient liquid-water content, and moderate updrafts ensures that coalescence processes can produce large raindrops, Johnson et al. (1986). The increase in deviation from the rain line from nearly 0 dB at 4.25 km AGL to 3.5 dB at 5.3 km AGL is correlated with the presence of ice.

This study now focuses attention on the deep convective area in Fig. 12 in the range interval 65–70 km. Figure 14b shows the deviation from the rain line within the main precipitation shaft. Below 2 km AGL

the deviation is 0 dB implying raindrops. The deviation increases significantly above 2.5 km AGL or a temperature of about 8°C . For the feeder cloud, the Munich sounding was used to arrive at a temperature corresponding to the important radar observables at a given height. For the main precipitation shaft, a reconstructed sounding profile was used, which is likely to be more realistic. Between 2.5 and 3 km AGL the deviation increases nearly linearly to about 5 dB. Thus, ice and melting ice must be mixed with raindrops above 2.5 km AGL. The 0°C level is close to 4.2 km AGL.

Figure 15 shows a scatterplot of Z_{DR} versus Z_H , the data being taken from the range interval 66–68 km and height interval 1.5–2.0 km. The Z_H within the main precipitation core is in the range 50–55 dBZ with Z_{DR} in the range 4–5.5 dB. For this reflectivity value, the Z_{DR} from gamma RSDs are in the range 2–4 dB, see Fig. 8a. Thus, it can be inferred that small, melting hail that appear as giant (larger than the maximum raindrop size) raindrops with a small, inner ice core are responsible for the observed data. These melting particles would appear oblate with axis ratio slightly larger (more spherical) than those of equilibrium shaped raindrops of the same volume equivalent spherical diameter, see Fig. 11. Because Z_{DR} is a reflectivity weighted parameter, the particle size effect overcompensates the effect of the larger axis ratio. The maximum hail diameter can also be inferred since it should be less than that size for which the melt water

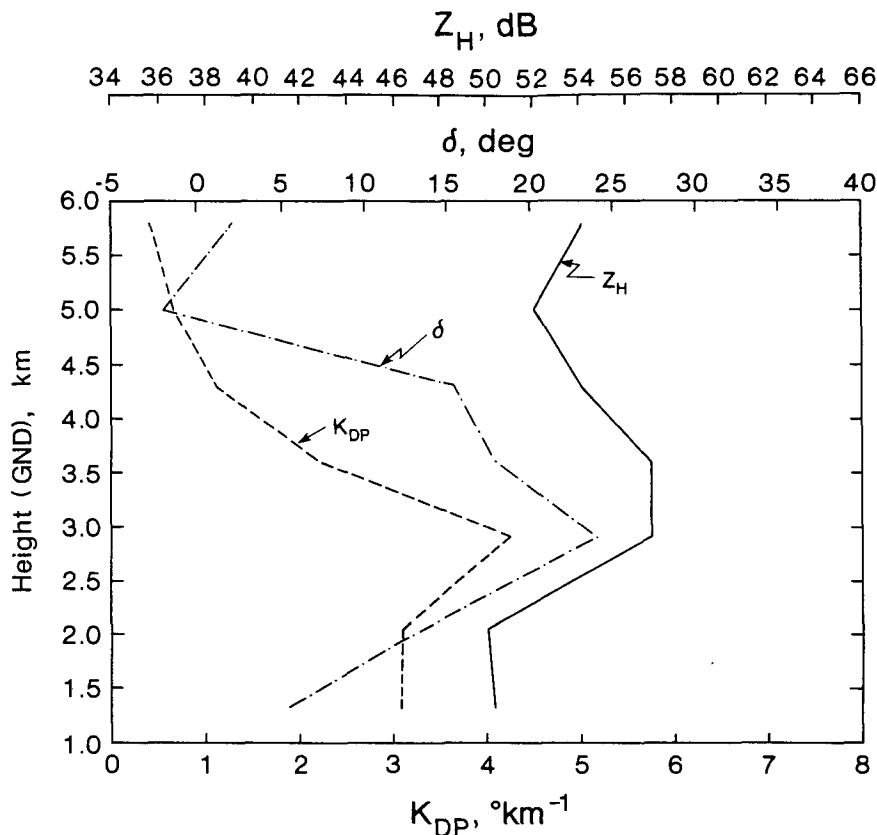


FIG. 16. Vertical profiles of reflectivity (Z_H), K_{DP} and δ obtained from time series measurements. Radar performed a RHI scan at 290° azimuth at 1316 UTC. Corresponding PPI scans shown in Fig. 5. Also, see the RHI scan shown in Fig. 7 about 4 min prior to the time series scan.

is shed, which is around 10 mm. This is the reason why in Fig. 14b the deviation from the rain line below 2 km AGL is 0 dB.

Further details of the precipitation process can be obtained from the vertical profiles of K_{DP} and δ shown in Fig. 16. These data were obtained at 1316:00 UTC along the azimuth 290° when the radar performed one RHI scan in the time series mode. This RHI scan intercepted the main core shown in the PPI scan of Fig. 5. The RHI scan shown in Fig. 7 at 285° azimuth also shows the vertical structure of Z_H about 4 minutes prior to the time series data collection. The data in Fig. 16 have been averaged in range over the interval 51.5–52.5 km. Note that the maximum values of Z_H , K_{DP} , and δ are 57 dBZ, $4.25^\circ \text{ km}^{-1}$, and 24° , respectively, the maxima occurring at a height of about 3 km AGL or a temperature of $\sim 6^\circ \text{C}$. Below 2 km AGL or 11°C both Z_H and K_{DP} are uniform at 50 dBZ and 3° km^{-1} , respectively, while δ decreases from 13° to 5° near the surface. The rain intensity (R), near the surface is estimated from the K_{DP} data as 50 mm h^{-1} using the C-band relation $R(K_{DP}) = 16.6 K_{DP}$, which is a mean relationship valid for gamma RSDs. Figure 9b shows that for gamma RSDs, a Z_H of 50 dBZ yields K_{DP} in

the range $2.5^\circ\text{--}4^\circ \text{ km}^{-1}$. Thus, the radar measured K_{DP} falls within this theoretical range. A $Z_H - R$ relation for convective rain of the form $Z_H = 400 R^{1.3}$ gives a rain intensity of 70 mm h^{-1} , Austin (1987) and Zrnić et al. (1989) show that a K_{DP} based estimate of rainfall is more stable than $Z_H - R$ in mixed phase precipitation. Also, Austin (1987) found that $Z_H - R$ relations consistently overestimated the rainfall in convective cells with $Z_H > 50 \text{ dBZ}$.

In Fig. 16 the height interval between 2–4 AGL or $10^\circ\text{C--}1^\circ\text{C}$ is interesting since it corresponds to a “bulge” in Z_H , K_{DP} , and δ . The steady, nearly linear increase in K_{DP} from (0°C) 4.2 km to a maximum at 3 km (7°C) height is noteworthy. This feature is consistent with the S-band K_{DP} data of Zrnić et al. (1989) in Oklahoma convective storms. The melting of ice into oblate shapes is the cause of K_{DP} increase below the 0°C level. The corresponding Z_H increase is due to the increase in dielectric constant from ice to water. The increase in δ from $\sim 5^\circ$ to a maximum of 25° near 3 km AGL is again interesting. Note that the measurement error in δ is estimated around $\pm 5^\circ$. Since gamma distributed raindrops cannot yield δ greater than about 12° , see Fig. 9a, it is inferred here that small

melting hail is responsible for these large δ values with shapes as given in Fig. 11. Note that partially melting hail will be oblate in shape with axis ratio larger (more spherical) than that of equilibrium-shaped raindrops of the same volume. In the next section model calculations are shown where δ from such melting hail is comparable to the radar measurements.

Below the level where Z_H , K_{DP} , and δ reach their maximum value, i.e., 3 km AGL or 7°C, all three observables decrease linearly until 2 km (11°C) with δ decreasing further until 1.5 km (13.5°C). The steady decrease in δ implies a reduction in the maximum particle size since δ is a measure of non-Rayleigh scattering effects. As the small hail particles melt completely by the time they reach the 2-km height, it is likely that collision-induced breakup of the corresponding giant raindrops occurs in the strong precipitation shaft. This effect causes both Z_H and K_{DP} to decrease in the height interval 3 to 2 km. Below 2 km the δ values are consistent with those calculated for gamma RSDs, see Fig. 9a.

d. Results from the hail melting model

The one-dimensional hail melting model developed by Rasmussen and Heymsfield (1987a,b) is used here for intercomparison with the radar measurements described in the previous section. The RH model is initialized with initial particle diameter, particle density, profiles of temperature and relative humidity, vertical air motion, and cloud water. The initial particle shape is assumed to be spherical and the initial density is 0.91 g cm^{-3} . Four hail particles were initialized at a height

of 4.7 km MSL (or 0°C) with diameters of 3, 5, 7.3, and 9 mm. Vertical air motion and cloud water were set to zero. Since the model results will be compared with vertical profiles of radar data in the region of the intense convective core of the squall line, a reconstructed vertical profile of temperature and relative humidity was used rather than the environmental sounding. The relative humidity was assumed to be 100% from 4.7 km MSL or 0°C to the surface. The temperature increases linearly from 0°C at 4.7 km MSL to 20°C at 0.5 km MSL. As shown by RH (1987b), the main effect of assuming a 100% relative humidity profile is that the particles melt much more quickly as compared to using the environmental sounding. At each height below the 0°C level, the model predicts particle diameter, ice core diameter (assuming spherical ice core), and particle axis ratio assuming that as the particle melts the shape is oblate, see RH (1987a). The particle-size distribution has not been considered because it is not known. Rather, the radar observables are calculated separately for the four particle sizes and compared with radar data.

Figure 17a shows plots of spherical ice core diameter versus height MSL for initial particle diameters (D) of 3, 5, 7.3, and 9 mm. An ice core diameter of zero implies fully melted raindrops. Complete melting occurs at 3.5, 2.9, 1.5, and 0.9 km MSL for the 3-, 5-, 7.3-, and 9-mm size particles, respectively. During melting the particle axis ratio is calculated by RH using wind tunnel data of Rasmussen et al. (1984). These model axis ratios cannot be used to compute radar observables because the model assumes that melt water can accumulate like a "tire" around the particles' equator,

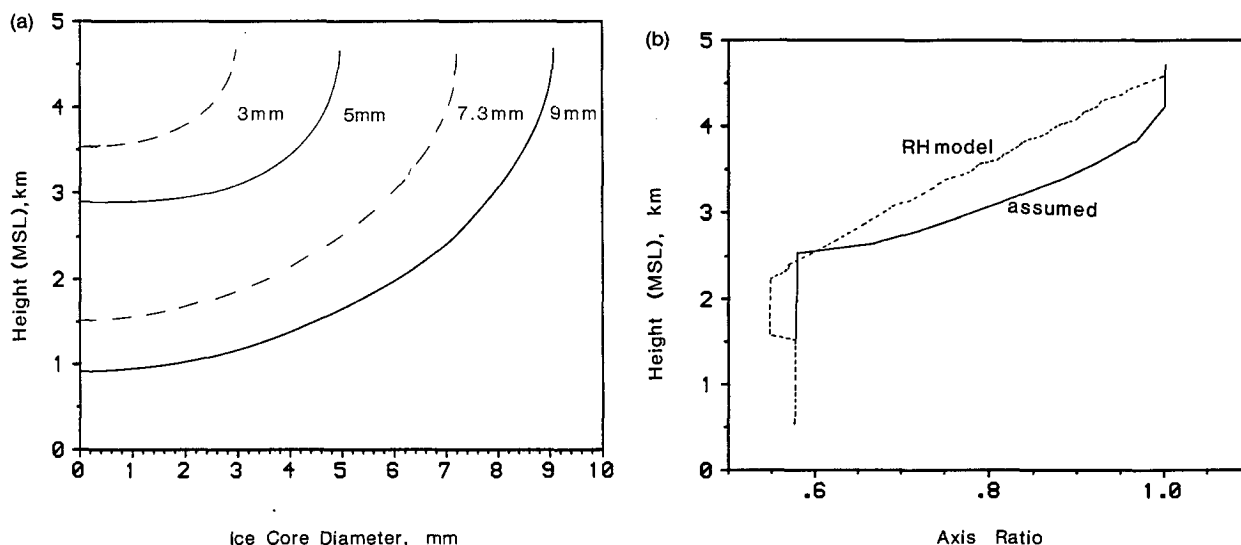


FIG. 17. (a) Vertical profile of ice-core diameter obtained from the hail melting model. Initial particle diameters are 3, 5, 7.3, and 9 mm. See Fig. 11 for schematic of hail melting shapes. The ice is spherical in shape. Complete melting occurs when the ice-core diameter equals zero. (b) Vertical profile of particle axis ratio for initial particle diameter of 7.3 mm. The dashed line refers to the melting model results. Solid line refers to recomputed axis ratio used in the scattering algorithm. Figure 11 shows the melting shapes.

whereas the scattering algorithm used here allows for a two-layer configuration provided that the inner ice core is completely surrounded by an oblate shell of melt water. For the large hail sizes $D \geq 5$ mm the model-predicted axis ratios of melting hail particles are too oblate for the calculated values of particle volume-equivalent diameter and inner ice core diameter, i.e., the ice core cannot be completely submerged within the oblate particle. In order to use our scattering algorithm based on the T matrix, (Bringi and Seliga 1977) the model-predicted axis ratios are altered, so that for a given volume-equivalent particle diameter and ice core diameter, the new axis ratio is computed assuming that the spherical ice core is just completely submerged within the oblate shell of melt water. Note that the spherical ice core and oblate shell of melt water are concentric, see Fig. 11. Figure 17b shows plots of model-predicted axis (dashed line) are recalculated axis ratio (solid line) as a function of height MSL for an initial particle diameter of 7.3 mm. In the height interval 4 to 2.5 km MSL, note that the model-predicted axis ratio is significantly less (or more oblate) than the recomputed axis ratio. Figure 11, referred to previously, shows the melting shapes for an initial particle size of 7.3 mm at the heights of 4.2, 3.4, 2.5, 2, and 1.5 km MSL. The particle volume-equivalent diameter and ice core diameter are from the RH model, whereas the axis ratios have been recomputed as explained above.

Figures 18a,b show the vertical profile of σ_{DR} (or Z_{DR} of individual particles) for initial particle sizes of (a) 3 and 5 mm, and (b) 7.3 and 9 mm. The peak $\sigma_{DR} \sim 9$ dB for the 7.3-mm particle at a height of 2.5 km MSL is noteworthy. The particle shape causing this very high σ_{DR} is shown in Fig. 11. The ice core is responsible for producing the large σ_{DR} . Computations without the ice core, i.e., assuming the particle is a

raindrop of the same diameter (7.3 mm) and axis ratio (0.6) gives $\sigma_{DR} = 4.8$ dB, see Fig. 10. In Fig. 18b, the 9-mm particle shrinks in size as it melts due to shedding. The final size at 0.5 km MSL is 8.22 mm. Thus, both the 7.3-mm and 9-mm particles give nearly the same σ_{DR} upon complete melting, see Fig. 10. The model results of Fig. 18 are in good agreement with the radar measurements shown in Figs. 14b and 15. From Fig. 17 it is noted that at heights less than about 2 km MSL the σ_{DR} for initial particle sizes up to 9 mm is uniform, which is in good agreement with Fig. 14b where the deviation from the rain line is 0 dB below 2 km AGL. It was noted earlier from Fig. 14b that above 2.5 km AGL the deviation from the rain line increased significantly. This is consistent with the model results of Fig. 18b from which it is clear that ice particles ≥ 6 mm are partially melting in the height interval 4.7 km MSL to around 2.5 km MSL which in turn could cause the observed deviation from the rain line in Fig. 14b. This deviation, by definition, would be most weighted by the reflectivity, i.e., the shapes of the largest particles.

Model results for the backscatter differential phase δ for particle sizes of 3 and 5 mm are shown in Fig. 19a while particle sizes of 7.3 and 9 mm are shown in Fig. 19b. The slightly negative $\delta \sim -5^\circ$ at 3.5 km MSL is noteworthy; this feature is also present in the 7.3 and 9-mm sizes. Below 3 km MSL, $\delta = 0^\circ$ for initial particle diameters ≤ 5 mm implying Rayleigh scattering for these sizes at C band. Figure 19b shows the effects of Mie scattering for the larger sizes. The peak $\delta \approx 35^\circ$ for the 7 mm particle at a height of 2.5 km is coincident with the peak σ_{DR} of 9 dB observed in Fig. 18b. These model results are consistent with the interpretation of radar measurements shown in Fig. 16, particularly the radar measured profile of δ . The maximum value of $\delta \sim 24^\circ$ was observed at 3 km AGL, which is consistent

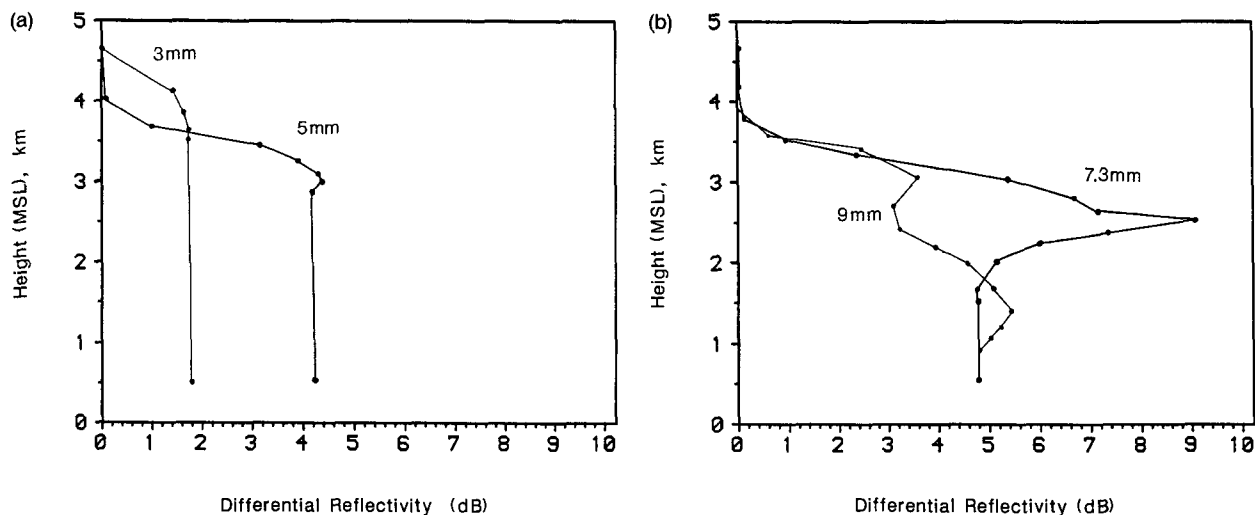


FIG. 18. (a) Vertical profiles of σ_{DR} or Z_{DR} of individual particles computed using the two-layer T -matrix scattering algorithm. Initial particle diameters are 3 and 5 mm. (b) As in (a), except initial particle diameters are 7.3 and 9 mm.

qualitatively with the model results of Fig. 19b. The radar data show a nearly linear increase of δ from 5° at 4.7 km AGL to 24° at 3 km AGL. Below this height, δ decreases linearly to 5° at 1.25 km AGL. The model results in Fig. 19b are generally consistent with these data. The linear decrease in observed δ below 3 km AGL was earlier interpreted to be due to breakup of the very large raindrops, i.e., a transition from Mie scattering to Rayleigh scattering. It appears reasonable to infer that below 1–1.5 km MSL the fully melted large raindrops would breakup due to collisions in the intense precipitation shaft. This would reduce δ as can be seen by comparing Fig. 19a with 19b.

Model calculations of radar parameters would also strongly depend on the form of the particle-size distribution as well as the maximum particle diameter. Because of the absence of the (large hail) Z_{DR} hail signature in the data and the fact that the deviation from the rain line was 0 dB below 2 km AGL, it is inferred that D_{\max} is around 9 to 10 mm. Larger-sized hail would shed melt water and thus remain spherical biasing Z_{DR} towards 0 dB. This was not observed in the data presented. Also, δ for large, tumbling hail would be close to 0° because they will appear quasi-spherical. The fact that measured δ was so high also implies small, melting hail with $D \leq 10$ mm. It is also suspected that the particle sizes contributing most to δ (i.e., the 7-mm sizes) should be in adequate concentrations so that the spectrum-averaged δ would also be large. Spectrum-averaged radar parameters were not computed using Eqs. (2) and (4) since $N(D)$ could be highly variable in the intense precipitation shaft. The presence of ice cores in the large raindrops would imply that breakup processes would have been inactive until the largest particles reached 1.5 km MSL. Thus, the raindrop-size distribution could not have reached an equilibrium

form. A downdraft would also have reduced the time to equilibrium. Since radar parameters such as Z_{DR} , K_{DP} , and δ depend on a number of variables it was decided to compute them using the RH model (coupled to the T -matrix scattering algorithm) for representative particle sizes only, and to show that these calculations are, in general, consistent with the radar observations presented earlier. Uncertainties in the model itself, such as not knowing the initial hail density and vertical air motions, add to the problems in intercomparing the model results with the radar observations other than in a general way.

5. Discussion and conceptual model

The synoptic analysis as well as the detailed meso-scale radar Doppler and radar polarimetric measurements provide insights for discussing the dynamical and especially the microphysical processes characterizing this squall line. Detailed measurements have been taken during a time period of more than two hours in which the overall system appeared to remain in a quasi-steady state of mature structure, despite its progression eastward. The initialization itself has not been observed in detail by radar measurements, but early stages are documented (Meischner 1989).

The synoptic-scale analysis as depicted for 1200 UTC in Fig. 4a has shown that lines of enhanced thunderstorm activity were embedded into the warm and unstable airmass well ahead of the cold front line and caused by synoptic-scale lifting. Melting and evaporation of the precipitation of more or less individual thunderstorms led to a substantial cooling of a surface layer, which expanded to the east. The heads of such more or less individual outflows merged to lines, parallel to the cold front line. Along these lines enhanced

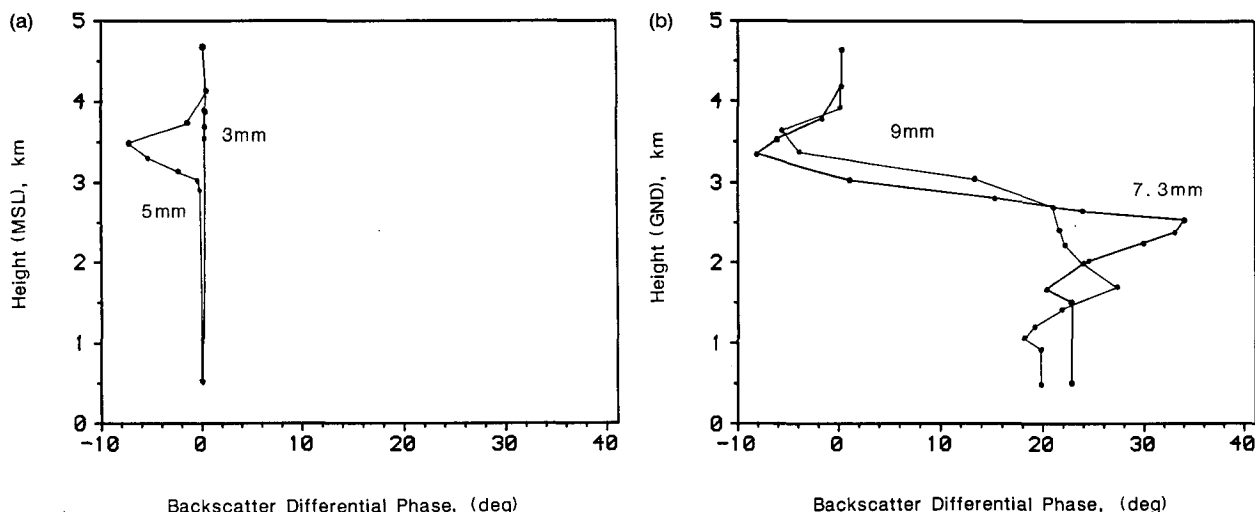


FIG. 19. (a) Vertical profiles of backscatter differential phase (δ) of individual particles computed using the two-layer T -matrix algorithm. Initial particle sizes of 3 and 5 mm are shown. (b) As in (a), except initial particle diameters of 7.3 and 9 mm are shown.

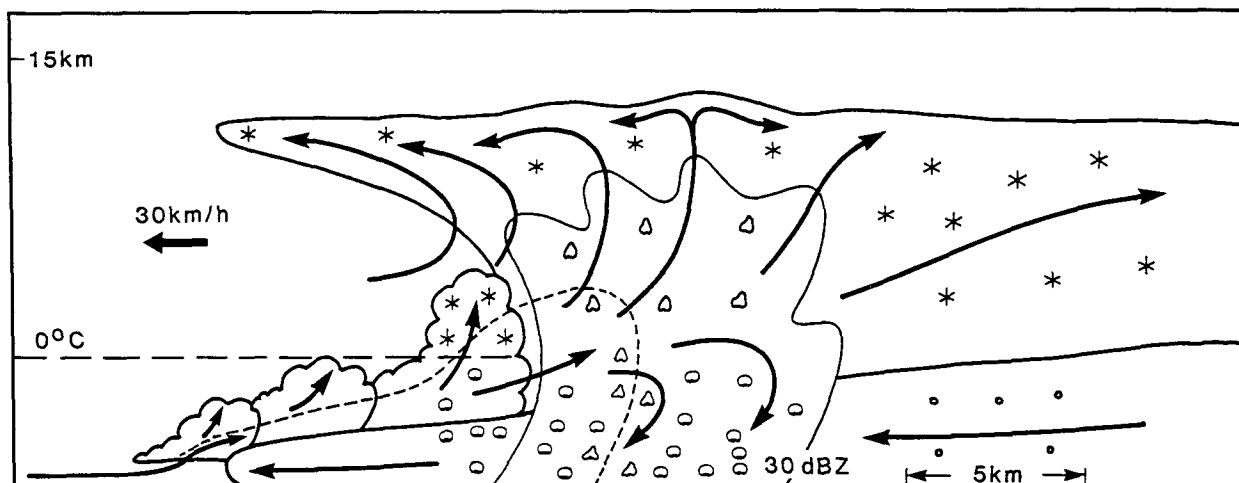


FIG. 20. Conceptual model of the squall line observed on 1 July 1987 in southern Bavaria. The cross section shows a deep cell in its mature stage with a well-developed anvil cloud. It is displayed in accordance with the radar cross sections. The system moves to the east, which is on the left side of this figure.

local lifting is forced again, destabilizing the conditional unstable air and such initializing strong convection. This organization of thunderstorms along a line now shows characteristic structures of a squall line. Once formed, their overall structure seems to be maintained for several hours by internal processes mainly. The decoupling from the main cold front line is substantiated by the facts that they moved under acceleration ahead of the cold front line and that "SL 2" in its southern part is influenced by the Alps. The cold front line itself moved almost continuously towards the southeast, see Fig. 4. The general structure of the leading edge of SL 2, which is the line of deep convective activity, can be described from the detailed radar observations. The combination of Doppler measurements and polarimetric measurements clearly showed the coupling between the precipitation formation process and the dynamical feature. A number of volume scans of Doppler measurements as well as polarimetric measurements have been analyzed. Their sum is the base for the conceptual model depicted in Fig. 20. The selected radar measurements were presented for illustrating typical structures.

Even though the squall line contains more or less isolated heavy convective cells connected with severe weather, large parts show a quasi-two-dimensional flow structure as demonstrated in Fig. 6. The main characteristics are the front inflow layer at low and mid-levels, the rear inflow extending underneath the front inflow and culminating in the low-level gust front circulation, and the high-level anvil outflow extending to the front and rear.

Newly growing cells embedded within the inflow area ahead of the main precipitation cores represent smaller updrafts. Heavy precipitation is formed at the leading edge of the line (in the eastern part), while the western

part is showing more or less a stratiform character with widespread precipitation. The heavy precipitation—a mixture of melting small hail and rain—hits the ground in a forward direction, thus contributing to the forward moving cool air pool or even controlling its strength.

The inclinations of the transition line between the front and rear inflows has been discussed to be indicative for the weakening of the circulation (Rotunno et al. 1988; Weisman et al. 1988). Further arguments for such a weakening can now be added by discussing the precipitation formation mechanism in connection with the air flow pattern.

Generally, the regeneration of the squall line was effected by the new growing cells ahead (to the east) of the system. Mostly these cells merged with the main line thus forming the new leading edge. It has been shown that these growing congestus clouds already produced big raindrops in a very low number concentration. Often these drops were also present in the supercooled parts of these clouds. Ice then formed in their top levels above 4 km AGL, see Figs. 12 and 14b.

The origin of larger ice particles aloft, their subsequent melting, and the droplet growth by coalescence is one possibility for the origin of the big drops. Another one is the presence of ultragiant condensation nuclei. These processes have been discussed, e.g., by Caylor and Illingworth (1987). Even though the present study can not clarify the origin of these big drops they have been observed very frequently in these feeder clouds merging with the main system.

The main precipitation was formed just in areas where such feeder cells merge with the main system. These areas are collocated with the main updraft. In other words, the merging feeder cell now explosively reaches a mature stage of deep convection thus forming

the new leading edge. Whether the frozen big drops, already grown in the feeder cells before merging, now act as hail embryos within the main updraft, remains speculative. On the other hand, it is clear that heavy precipitation grows within the inflow region forming the leading edge of the system where the feeder cells are going to merge with the older cells between 5 and 10 km AGL. Here the largest hail signals have commonly been recorded. For one selected vertical profile the mean size of the ice particles formed was estimated to be around 10 mm in diameter, see section 5d.

These ice particles, after having reached their final sizes in dependence of the actual updraft speed and the LWC available, fall first within the slant frontal inflow and then within the wedge shaped rear inflow surface layer. Cooling by melting and evaporation contributes to the surface cold pool. The forward forcing is indicated by the gusts, which are clearly connected with the precipitation hitting the ground, see Fig. 7 for an example.

Figure 5a shows a situation where the gust front has already proceeded about 20 km ahead of the main precipitation cores. In such situations new isolated convective cells grow well ahead of the older ones, often not merging with them. This stage is illustrated in Fig. 21 as a three-panel figure of (a) reflectivity, (b) the hail signature and (c) the differential reflectivity for 1324:19 UTC. The "feeder cloud" at range 45 km itself has developed to the precipitating state indicated by enhanced reflectivity values up to more than 40 dBZ aloft connected with ice. The quantity $H_{DR} > 0$ is noted at the top of this cell. Nearer to the main system at range 51 km and up to 58 km, the highest reflectivity cores occur below the height of 2.5 km AGL. Heavy rain and possibly some small melting hail or graupel reach the ground.

The precipitation in the main core in this situation is much less intense as compared with situations where the feeder cells are coupled more closely with the main system. Especially the normally observed location of hail formation, which for this situation would be expected to be near 55 km between 5 and 10 km AGL, shows only low reflectivity values and a low hail signal. It is possible to speculate from this finding that if the feeder cells are decoupled from the main system by the forward accelerated cold pool then the process of forming heavy precipitation is decreased. A further consequence of the decrease in precipitation intensity would be a decreased contribution to the cold air pool and a deceleration of the gust front. This feedback mechanism might be of importance in maintaining the squall line system in an optimal state and explaining its longevity. Further, an oscillation in system strength as discussed by Rotunno et al. (1988) and Weisman et al. (1988)—who took the vertical velocity as indicator for the system strength—can be explained that way. Thus, the period should be of the life cycle order of one individual strong convective cell.

The longevity of this squall line system or at least of the most active part of it is documented by the hail swath reported on the ground, see Fig. 22. These reports include an event showing some similarities with a wet downburst. Only local damage in a forest with trees broken down in an area covering approximately 80 m in diameter was reported around 1210 UTC. The event was connected with hail on the ground. The reported details such as the short duration of the event, the small damage area, and the fall direction of the trees are indicative of a wet downburst. Srivastava (1987) has discussed conditions for intense downdrafts driven only by melting and evaporation of precipitation. He concludes that intense downbursts are possible without further assumptions on any dynamical mechanism. The most important parameters are the lapse rate, the precipitation intensity, and the presence of melting ice. The more stable the lapse rate is the heavier the precipitation must be to make a downburst possible. For example, Srivastava (1987) states that, "for a lapse rate of 5.0 K km^{-1} a downburst is practically impossible. At 6.0 K km^{-1} , it can occur with very heavy liquid precipitation aloft (rainfall rate $> 100 \text{ mm h}^{-1}$) and under less wet conditions if the precipitation is in the form of ice." These rather quantitative conclusions are formulated under the assumption of a high cloud base of 4 km AGL and more. The qualitative conclusions, however, are argued to be robust with the general supplement that for lower cloud bases the precipitation needs to be more intense and that higher concentrations of smaller ice particles are further favorable for a downburst formation.

For the observed areas of heavy precipitation a lapse rate of 6 K km^{-1} seems realistic. The cloud base was near 2 km AGL. The measured radar reflectivity factors typically exceeding 55 dBZ (corresponding to a rain rate in excess of 100 mm h^{-1}) and the measured radar parameters discussed in section 4c indicate a mixture of rain and small (10-mm diameter) melting hail. Thus it is not unlikely that the precipitation loaded downdrafts, as observed by the Doppler measurements (see Fig. 7), occasionally occur as a wet downburst. The microburst itself has not been observed by the radar.

6. Conclusions

The synoptic-scale analysis of a squall line event in southern Germany showed a strong influence of frontal forcing processes on the large-scale organization of the convection. Once formed, the organized line of deep convective activity is accelerated away and ahead of the cold front line and the longevity is governed more by internal circulation processes. In later stages of development there was some indication of an orographic influence on the orientation and propagation speed.

Radar polarimetric and Doppler measurements of the squall line system during several hours provided

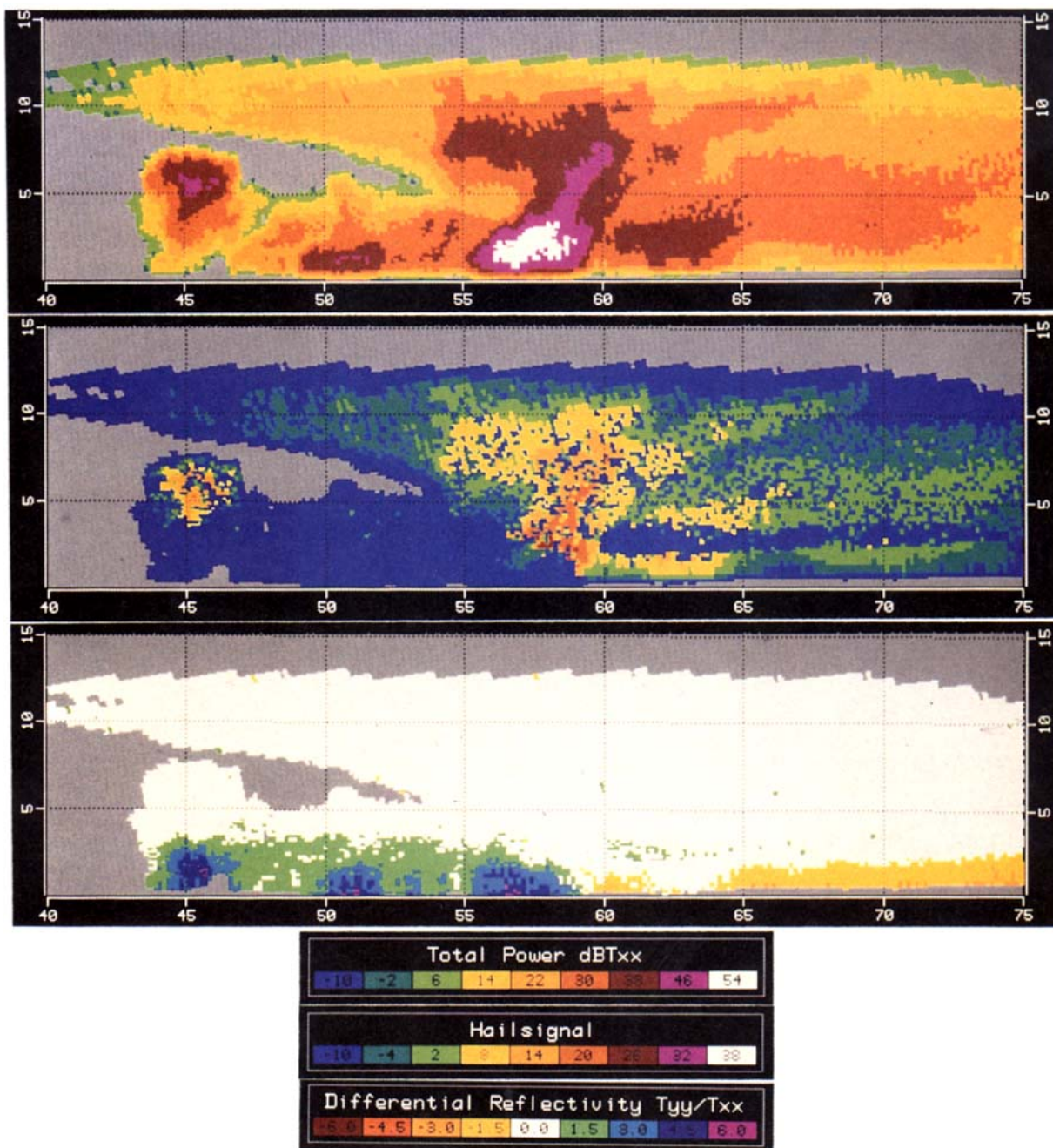


FIG. 21. Vertical cross section (RHI) of reflectivity or total backscattered power (top), hail signature (middle), and Z_{DR} (bottom) for 1324:19 UTC along the 285° azimuth. Cumulus clouds initiated about 15 km ahead of the line of deepest convection already are producing precipitation via the ice phase. The ice particles formed there are not advected into the main updraft, thus, they do not contribute to the hail formation process as hail embryo particles.

us with insights into the dynamical structure of the line as well as into the growth mechanisms of heavy precipitation. The flow pattern generally conforms to a two-dimensional structure showing perturbations in the form of heavy convective cells. Some of these produced hail at the ground, and even a microburst with tree damage on the ground was observed. The system was

characterized by a wedge-shaped surface cool air pool moving eastward, the slantwise westward inflow of unstable moist air with embedded developing cumulus clouds just ahead of the main precipitation cores, and widespread precipitation in the rear. The eastward moving surface cool air pool is forced by the falling melting and evaporating heavy precipitation to some

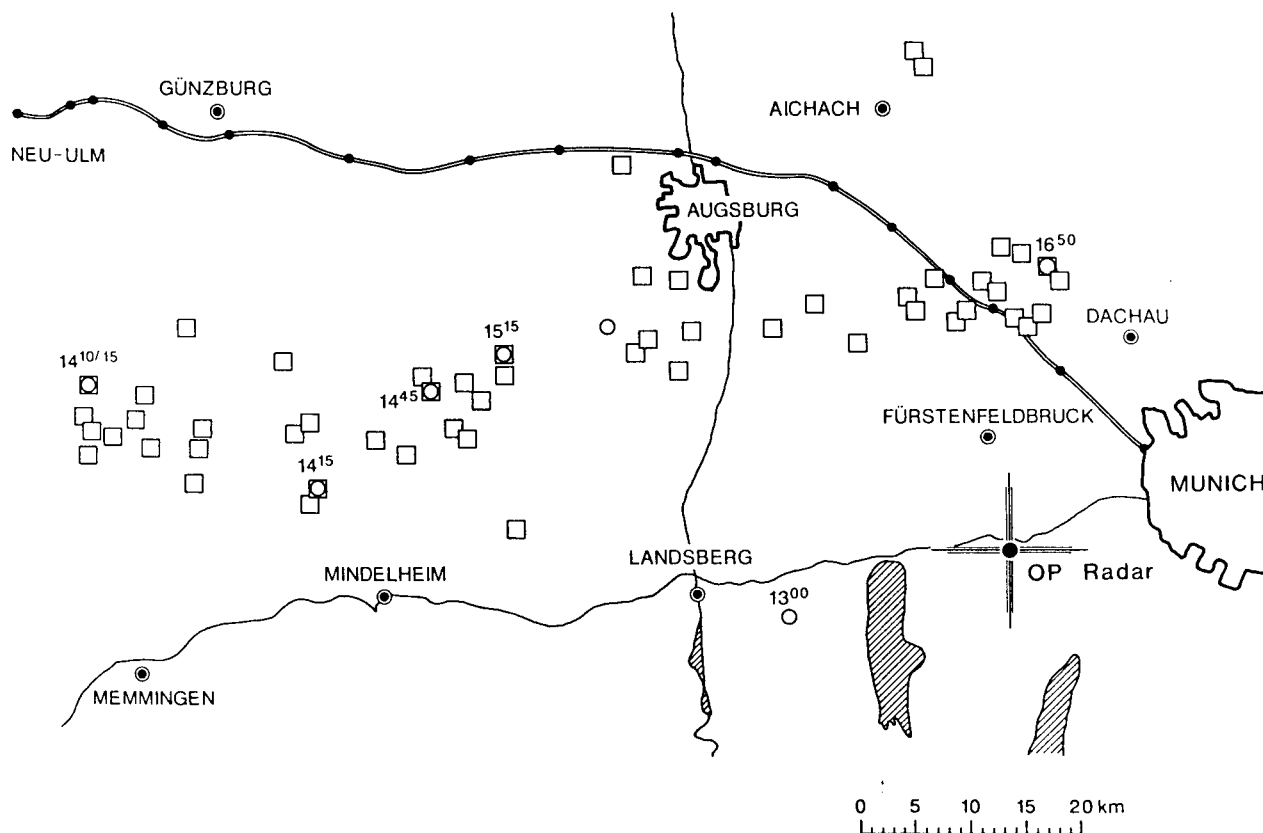


FIG. 22. Hail reported at the ground by the German Weather Service (circles) and hail assurance companies (squares).

extent. Thus, the intensity of the precipitation may cause acceleration or deceleration of the gust front and its position to the line of deepest convection and as such provide a feedback mechanism explaining the longevity of the overall squall line structure.

The details of the precipitation structure have been deduced by advanced polarimetric measurements. The combined use of the reflectivity factor, the differential reflectivity, the difference reflectivity, the specific differential phase, and the backscatter differential phase allowed this study to distinguish between pure rain and rain-hail mixtures to follow the hail melting process and to estimate the hail sizes. The newly grown cells often contain big raindrops in relatively low concentrations, a feature that has been observed frequently on this day, but which is not typical for the majority of hailstorms observed in southern Germany so far.

Apart from the interesting results on squall line development and the related precipitation growth demonstrated in this study, many questions still remain unanswered. Among these are the origin of the big drops in the feeder clouds and their role in the hail forming process, the time evolution of single hail cells that can only be followed by highly resolved radar scans, or a more complete picture of the squall line dynamics, especially the location of updrafts and

downdrafts, which can only be deduced by a multi-Doppler analysis.

Acknowledgments. The outstanding engagement of F. Ritenberg, H. Scheffold, E. Clemens, and the late W. Holfeuer in operating and maintaining the POLDIRAD system is greatly acknowledged. Especially the continuous technical discussions with A. Schroth and his group and their efforts guarantee the system to be on a high standard. Thanks are due to G. Jacob, I. Stühler, and G. Steudel for carefully preparing the figures and A. Walliczek for their patience in typing drafts and manuscripts. One of the authors (VNB) acknowledges support from the National Science Foundation via ATM-8703126 and ATM-8915141. The author is also grateful to Colorado State University (CSU) for providing resources which enabled him to spend his sabbatic leave at DLR. Mr. John Hubbert of CSU developed the software for deducing K_{DP} and δ from the time series measurements. The German Weather Service (DWD) is acknowledged for contributing the synoptic data and the atmospheric soundings.

REFERENCES

- Austin, P. M., 1987: Relation between measured radar reflectivity and surface rainfall. *Mon. Wea. Rev.*, **115**, 1053–1071.

- Aydin, K., T. A. Seliga and V. Balaji, 1986: Remote sensing of hail with a dual-linear polarization radar. *J. Clim. Appl. Meteor.* **25**, 1475–1484.
- Beard, K. V., 1984: Oscillation models for predicting raindrop axis and backscatter ratios. *Radio Sci.*, **19**, 67–74.
- , and D. Chuang, 1987: A new model for the equilibrium shape of raindrops. *J. Atmos. Sci.*, **44**, 1509–1525.
- Betts, A. K., 1976: The thermodynamic transformation of the tropical subcloud layer by precipitation and downdrafts. *J. Atmos. Sci.*, **33**, 1008–1020.
- Brewster, K. A., and D. S. Zrnić, 1986: Comparison of eddy dissipation rates from spatial spectra of Doppler velocities and Doppler spectrum widths. *J. Atmos. Ocean. Tech.*, **3**, 440–452.
- Bringi, V. N., and T. A. Seliga, 1977: Scattering from nonspherical hydrometeors. *Ann. Telecommunications*, **32**, 392–397.
- , and P. Meischner, 1988: Radar remote sensing of melting hail. Tenth International Cloud Physics Conference, Bad Homburg, *Annalen Meteorol.*, **25**, 455–457.
- , T. A. Seliga and K. Aydin, 1984: Hail detection with a differential reflectivity radar. *Science*, **225**, 1145–1147.
- , R. M. Rasmussen and J. Vivekanandan, 1986a: Multiparameter radar measurements in Colorado convective storms. Part I: Graupel melting studies. *J. Atmos. Sci.*, **43**, 2545–2563.
- , J. Vivekanandan and J. D. Tuttle, 1986b: Multiparameter radar measurements in Colorado convective storms. Part II: Hail detection studies. *J. Atmos. Sci.*, **43**, 2564–2577.
- Brown, J. M., 1979: Mesoscale unsaturated downdrafts driven by rainfall evaporation: A numerical study. *J. Atmos. Sci.*, **36**, 313–338.
- Caylor, I. J., and A. J. Illingworth, 1987: Radar observations and modeling of warm rain initiation. *Quart. J. Roy. Met. Soc.*, **113**, 1171–1191.
- Chong, M., P. Amayenc, G. Scialom and J. Testud, 1986: A tropical squall line observed during COPT 81 experiment in West Africa. Part I: Kinematic structure inferred from dual-Doppler radar data. *Mon. Wea. Rev.*, **115**, 670–694.
- Golestani, Y., V. Chandrasekar and V. N. Bringi, 1989: Intercomparison of Multiparameter Radar Measurements. *Proc. 24th AMS Conference Meteorology*, Tallahassee, Amer. Meteor. Soc., 309–314.
- Green, A. W., 1975: An approximation for the shape of large raindrops. *J. Appl. Meteor.*, **14**, 1578–1583.
- Hall, M. P. M., J. W. F. Goddard and S. M. Cherry, 1984: Identification of hydrometeors and other targets by dual-polarization radar. *Radio Sci.*, **19**, 132–140.
- Husson, D., and Y. Pointin, 1989: Quantitative estimation of the hailfall intensity with a dual polarization radar and a hailpad network. *Proc. 24th AMS Conference Radar Meteorology*, Tallahassee, Amer. Meteor. Soc., 318–321.
- Illingworth, A. J., J. W. F. Goddard and S. M. Cherry, 1986: Detection of hail by dual-polarization radar. *Nature*, **320**, 431–433.
- , and —, 1987: Polarization studies of precipitation development in convective storms. *Quart. J. Roy. Met. Soc.*, **113**, 469–489.
- Istok, M. J., and R. J. Doviak, 1986: Analysis of the relation between Doppler spectral width and thunderstorm turbulence. *J. Atmos. Sci.*, **43**, 2199–2214.
- Jameson, A. R., 1983: Microphysical interpretation of multiparameter radar measurements in rain. Part I: Interpretation of polarization measurements and estimation of raindrop shapes. *J. Atmos. Sci.*, **40**, 1792–1802.
- , and E. A. Mueller, 1985: Estimation of propagation differential phase shift from sequential orthogonal linear polarization radar measurements. *J. Atmos. Oceanic Tech.*, **2**, 133–137.
- Johnson, D. B., K. V. Beard and D. Baumgardner, 1986: Airborne observations of raindrop size-distributions in Hawaiian clouds. Preprints, *AMS Conference on Cloud Physics*, Vol. 2, Snowmass, Amer. Meteor. Soc., 48–51.
- McCormick, G. C., L. E. Allan and A. Hendry, 1979: The backscatter matrix of ice samples: Its relation to identification of hail by radar. *J. Appl. Meteor.*, **18**, 77–84.
- Meischner, P., 1989: Observations of dynamical and microphysical aspects related to hail formation with the polarimetric Doppler radar Oberpfaffenhofen. *Theor. Appl. Meteor.*, **40**, 209–226.
- Meyer, W., and T. Jank, 1989: Dopplerspektren aus inkohärenter Rückstreuung: Prinzip und anwendungsbeispiele. DLR-FB 89-48. English translation: ESA-TT-1197, 1990, 59 pp.
- Mueller, E. A., 1984: Calculation procedure for differential propagation phase shift. Preprints, *22nd AMS Conference on Radar Meteorology*, Zürich, Amer. Meteor. Soc., 397–399.
- Rasmussen, R. M., and A. J. Heymsfield, 1987a: Melting and shedding of graupel and hail. Part I: Model physics. *J. Atmos. Sci.*, **44**, 2754–2763.
- , and —, 1987b: Melting and shedding of graupel and hail. Part II: Sensitivity study. *J. Atmos. Sci.*, **44**, 2764–2782.
- , V. Levizzan and H. R. Pruppacher, 1984: A wind tunnel and theoretical study of the melting behavior of atmospheric ice particles. Part III: Experiment and theory for spherical ice particles of radius $<500\ \mu\text{m}$. *J. Atmos. Sci.*, **41**, 381–388.
- Redelsperger, J. L., and J. P. Lafore, 1987: A three-dimensional simulation of a tropical squall line: convective organization and thermodynamic vertical transport. *J. Atmos. Sci.*, **45**, 1334–1356.
- Rotunno, R., J. B. Klemp, and M. L. Weisman, 1988: A theory for strong, long-lived squall lines. *J. Atmos. Sci.*, **45**, 463–485.
- Roux, F. J., 1987: The West African squall line observed on 23 June 1981 during COPT 81: Kinematics and thermodynamics of the convective region. *J. Atmos. Sci.*, **45**, 406–426.
- , J. Testud, M. Payen and Bernard Pinty, 1984: West African squall line thermodynamic structure retrieved from dual-Doppler radar observations. *J. Atmos. Sci.*, **41**, 3104–3121.
- Sachidananda, M., and D. S. Zrnić, 1986: Differential propagation phase shift and rainfall rate estimation. *Radio Sci.*, **21**, 235–247.
- , and —, 1987: Rainrate estimated from differential polarization measurements. *J. Atmos. Ocean. Tech.*, **4**, 588–598.
- Schroth, A. C., M. S. Chandra and P. F. Meischner, 1988: A C-band coherent polarimetric radar for propagation and cloud physics research. *J. Atmos. Ocean. Techn.*, **5**, 804–822.
- Seliga, T. A., and V. N. Bringi, 1976: Potential use of radar differential reflectivity measurements at orthogonal polarizations for measuring precipitation. *J. Appl. Meteor.*, **15**, 69–76.
- Smull, B. F., and R. A. Houze, 1987: Rear inflow in squall lines with trailing stratiform precipitation. *Mon. Wea. Rev.*, **115**, 2869–2889.
- Srivastava, R. C., 1987: A model of intense downdraft driven by the melting and evaporation of precipitation. *J. Atmos. Sci.*, **44**, 1752–1773.
- Tuttle, J. D., V. N. Bringi, H. D. Orville and F. J. Kopp, 1989: Multiparameter radar study of a microburst: Comparison with model results. *J. Atmos. Sci.*, **46**, 601–620.
- Ulbrich, C. W., 1983: Natural variations in the analytical form of raindrop-size distributions. *J. Climate Appl. Meteor.*, **22**, 1764–1775.
- Wakimoto, R. M., and V. N. Bringi, 1988: Dual-polarization observations of microbursts associated with intense convection: The 20 July storm during the MIST Project. *Mon. Wea. Rev.*, **116**, 1521–1539.
- Weismann, U. M., J. B. Klemp and R. Rotunno, 1988: Structure and evolution of numerically simulated squall lines. *J. Atmos. Sci.*, **45**, 1990–2013.
- Zipser, E. I., 1977: Mesoscale and convective-scale downdrafts as distinct components of squall line structure. *Mon. Wea. Rev.*, **105**, 1586–1589.
- Zrnić, D. S., N. Balakrishnan and M. Sachidananda, 1989: Polarimetric measurements to determine the amounts of rain and hail in a mixture. *Proc. 24th AMS Conference Radar Meteorology*, Tallahassee, Amer. Meteor. Soc., 396–400.